



## Geochemistry, Geophysics, Geosystems

### RESEARCH ARTICLE

10.1002/2015GC005961

#### Key Points:

- We develop new algorithm to model crustal and upper mantle density from geophysical data
- Body forces and far-field stress, not a thermal plume, caused MCR rifting and subsequent contraction
- Lithostatic pressure gradients can either encourage or discourage intraplate seismicity

#### Supporting Information:

- Supporting Information S1

#### Correspondence to:

W. Levandowski,  
wlevandowski@usgs.gov

#### Citation:

Levandowski, W., O. S. Boyd, R. W. Briggs, and R. D. Gold (2015), A random-walk algorithm for modeling lithospheric density and the role of body forces in the evolution of the Midcontinent Rift, *Geochem. Geophys. Geosyst.*, 16, doi:10.1002/2015GC005961.

Received 15 JUN 2015

Accepted 16 OCT 2015

Accepted article online 23 OCT 2015

## A random-walk algorithm for modeling lithospheric density and the role of body forces in the evolution of the Midcontinent Rift

Will Levandowski<sup>1</sup>, Oliver S. Boyd<sup>1</sup>, Rich W. Briggs<sup>1</sup>, and Ryan D. Gold<sup>1</sup>

<sup>1</sup>U.S. Geological Survey, Golden, Colorado, USA

**Abstract** This paper develops a Monte Carlo algorithm for extracting three-dimensional lithospheric density models from geophysical data. Empirical scaling relationships between velocity and density create a 3-D starting density model, which is then iteratively refined until it reproduces observed gravity and topography. This approach permits deviations from uniform crustal velocity-density scaling, which provide insight into crustal lithology and prevent spurious mapping of crustal anomalies into the mantle. We test this algorithm on the Proterozoic Midcontinent Rift (MCR), north-central United States. The MCR provides a challenge because it hosts a gravity high overlying low shear-wave velocity crust in a generally flat region. Our initial density estimates are derived from a seismic velocity/crustal thickness model based on joint inversion of surface-wave dispersion and receiver functions. By adjusting these estimates to reproduce gravity and topography, we generate a lithospheric-scale model that reveals dense middle crust and eclogitized lower-most crust within the rift. Mantle lithospheric density beneath the MCR is not anomalous, consistent with geochemical evidence that lithospheric mantle was not the primary source of rift-related magmas and suggesting that extension occurred in response to far-field stress rather than a hot mantle plume. Similarly, the subsequent inversion of normal faults resulted from changing far-field stress that exploited not only warm, recently faulted crust but also a gravitational potential energy low in the MCR. The success of this density modeling algorithm in the face of such apparently contradictory geophysical properties suggests that it may be applicable to a variety of tectonic and geodynamic problems.

### 1. Introduction

The density of the crust and mantle lithosphere supports topography, reflects variations in temperature and lithology, and generates stress within the lithosphere. Hence, knowledge of the 3-D density structure of a region provides insight into not only its temperature and composition but also its tectonic history and modern state of stress. Since gravity anomalies arise from lateral density variations, and since there is a well-known correlation between seismic velocity and density, these two quantities have long been used to estimate lithospheric density structure [e.g., Sheehan and Solomon, 1991; Blakely, 1996; Jones et al., 1996; Kaban et al., 2003; Hasterok and Chapman, 2007; DeNosaquo et al., 2009; Mooney and Kaban, 2010; Afonso et al., 2013]. Areas of low relief with heterogeneous gravity and seismically variable lithosphere such as the central and eastern United States, however, can provide a challenge to such efforts because valid density models must recover gravity and topography without invoking thermal or compositional heterogeneity that is incompatible with seismic velocity or heat flow.

Deployment of the USArray across the United States provides an unprecedented opportunity to characterize the crust and upper mantle beneath North America with uniform techniques and resolution. Many previous attempts to map lithospheric density [Jones et al., 1996] or mantle composition [Mooney and Kaban, 2010; Kaban et al., 2014] using seismic velocity models have had to rely on interpolating scattered refraction interpretations in the crust. Increasing resolution of mantle tomography during the past decade has allowed the incorporation of 3-D mantle models [e.g., Mooney and Kaban, 2010; Kaban et al., 2014], though these have underlain the interpolated active-source crustal models rather than a crustal model that was jointly derived. This discontinuity in the origin of the seismic models introduces the possibility that crustal structure may lead to misinterpretations of mantle variations. Additionally, crustal density has generally been fixed to that which is estimated from empirical or lab-derived relationships [e.g., Christensen and Mooney, 1995;

Brocher, 2005]. When such scaling has not reproduced topography and/or long-wavelength gravity, the residuals have been ascribed to mantle density variations. While this assignment is potentially valid, there remains the possibility that systematic biases in the crustal velocity-density relationship have been mapped into mantle density variations.

This study presents a new method to estimate lithospheric-scale density structure from seismic velocity models and observed variations in gravity and topography. Uniformly derived seismic velocity models (in this study from the surface to 150 km depth), heat flow, and empirical scaling relations between velocity and density provide a three-dimensional starting density structure. An iterative Monte Carlo algorithm then adjusts this model via a series of random walks in order to also reproduce gravity and topography. The Mid-continent Rift (MCR) of the north-central United States serves as a testing ground for this approach, where the coincidence of high gravity, low seismic velocity, and minimal topographic relief present a challenge to the generation of a viable crustal and upper mantle density model. Ultimately, these density models provide insight into the involvement of the crust and mantle lithosphere in intraplate rifting and the tectonic setting of large deformation in a continental interior.

## 2. The Midcontinent Rift: Geology and Proposed Tectonic Histories

The MCR is a failed Grenville-aged (1.1 Ga) rift that extends northeastward from the Mesoproterozoic Mazatzal block in eastern Kansas, across Iowa into the Paleoproterozoic Yavapai province and along the northern coast of Lake Superior in Minnesota in the Archean Superior craton (Figure 1a). The rift cut across preexisting terrane boundaries and thus extension presumably did not exploit an inherited zone of weakness. The MCR now manifests as a magnetic anomaly, limited mafic outcrops, a prominent gravity high (Figure 1a), and flanking sedimentary basins (low gravity regions in Figure 1a), but it lacks a topographic expression (Figure 1b). An eastern arm of the rift extends southeastward from Lake Superior across Michigan, but the gravity signature of this arm is substantially smaller; we focus on the more pronounced western arm.

It is generally accepted that rifting was divided into two brief phases [Davis and Green, 1997; Miller et al., 2002] of rapid extension and extensive volcanism (1109–1106 Ma and 1100–1094 Ma), but there was relatively little magmatism between these two phases [Weiblen and Morey, 1980]. Volcanism is dominantly mafic, though later-stage rocks host minor felsic units [Green, 1982; Paces, 1988; Wirth et al., 1997]. The early phase magmas sourced in near-primitive ( $\epsilon_{\text{Nd}} \sim 0$ ) garnet pyroxenite and garnet peridotite at depths between 100 and 200 km; after the 6 Myr hiatus, however, spinel peridotite is the dominant magma source, with melting depths generally between 40 and 70 km [Nicholson et al., 1997]. As such, there is consensus that primitive mantle material was the primary source of magma.

Within 20 Myr of the cessation of rifting [Bornhorst et al., 1988; Cannon and Hinze, 1992] contraction thickened the crust beneath and adjacent to the rift [Behrendt et al., 1990], locally to more than 50 km [e.g., Shen et al., 2013b]. If such thickening occurred under pure shear, the mafic intrusions within the lower crust of the rift would have been advected to eclogite facies [e.g., Green and Ringwood, 1967a]. Active-source seismic experiments [Behrendt et al., 1988; Serpa et al., 1984; Behrendt et al., 1990; Woelk and Hinze, 1991] have identified a swath of high P-velocity (>7 km/s) crust beneath the rift to depths of 20 km to 40 km or deeper that is somewhat wider than the near-surface system of grabens and half-grabens. Merino et al. [2013] showed that a lower crustal rift pillow 20–30 km thick with density 330 kg/m<sup>3</sup> greater than surrounding crust could indeed reproduce the observed gravity anomaly.

Although the gravity data require that the western arm of the MCR have a large positive crustal density anomaly, it carries no surface topographic signature. Furthermore, shear-velocity ( $v_{sv}$ ) models derived jointly from short-period ambient noise and ballistic (to 80s period) surface wave dispersion and receiver functions (Figure 1c) collocate low crustal velocities with the MCR [Shen et al., 2013b]. Thus the MCR region presents a challenge to existing methods to estimate 3-D density structure from geophysical data and can serve as a proving ground for new approaches that leverage the uniform seismic coverage afforded by the Transportable Array and denser, more focused seismic experiments. Additionally, there remain competing hypotheses regarding the physical role of the primitive mantle plume in rift initiation and cessation, and these hypotheses make different predictions about the impact of rifting on the mantle lithosphere [Ziegler and Cloetingh, 2004, and references therein]. Although there is consensus that most of the MCR volcanics were derived from primitive mantle material, the physical role of this material in rifting depends largely on its

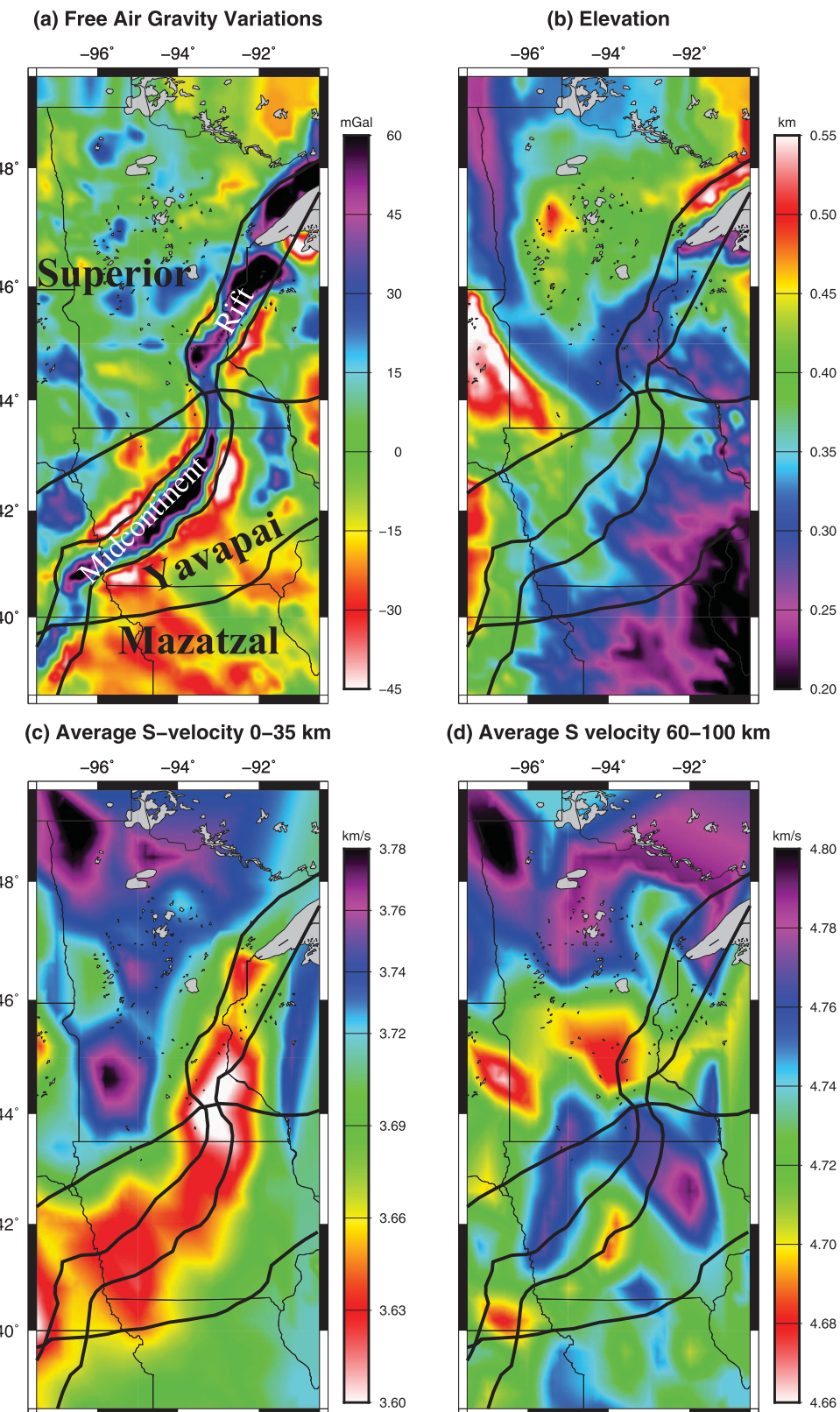


**Figure 1.** On all maps, bold black lines delineate province boundaries (labeled in Figure 1a). (a) Observed free air gravity, with the mean removed, and interpolated to a  $30 \text{ km} \times 30 \text{ km}$  grid. (b) Surface elevation, interpolated to a  $30 \text{ km} \times 30 \text{ km}$  grid, not smoothed to account for lithospheric flexural strength. (c) Average shear-wave velocity, surface to 35 km depth, of Shen et al. [2013b]. (d) Average shear-wave velocity, 60–100 km depth, of Shen et al. [2013b].

temperature. (Hereafter, we shall restrict the use of “plume” to situations in which the upwelling mantle material is anomalously hot.)

In the “active rifting” conception, extension results from the arrival of a hot mantle plume at the base of the lithosphere. The plume’s thermal buoyancy would increase surface elevation and thus the gravitational potential energy of the lithosphere above it, increasing horizontal tensional stress and leading to gravitational collapse [Nicholson and Shirey, 1990; Shirey et al., 1994; Vervoort et al., 2007]. The high-temperature plume partially melts the mantle lithosphere [Ellam et al., 1992; Saunders et al., 1992], preferentially extracting iron, garnet/spinel, and clinopyroxene from the mantle lithosphere, leaving behind a chemically and compositionally buoyant residue [e.g., Jordan, 1978]. If plume-generated extension additionally requires thermal weakening of the lithosphere due to diffusion of heat from the mantle plume [Kent et al., 1992], a process requiring at least tens of Myr [White and McKenzie, 1989], then the degree of lithospheric melt-depletion should be greater. Similarly, thick ( $>150$  km) mantle lithosphere is likely to be more substantially melt-depleted by an impinging plume [Hawkesworth et al., 1992]. After the cessation of magmatism and diffusion of heat, the density of newly depleted mantle lithosphere beneath the rift should be lower than its surroundings. If the mantle lithosphere beneath and adjacent to the rift is less dense than surrounding material of similar age, then it is reasonable to conclude that a thermal plume was responsible both for such depletion and for MCR extension.

An alternative hypothesis, “passive rifting,” suggests that far-field stresses associated with the Grenville Orogeny (the assembly of Rodinia) [McWilliams and Dunlop, 1978; Gordon and Hempton, 1986] or the rifting of Amazonia from Laurentia [Stein et al., 2014] could have generated differential motion of microplates in the interior of Laurentia. This extension would have provided space for primitive material to upwell and decompression melt [Ziegler, 1988; Pedersen and Ro, 1992; Roca, 2001], and the associated normal faults could have acted as efficient conduits. Since the MCR’s extension was rapid [e.g., Hutchinson et al., 1990; Paces and Miller, 1993], this ascending magma would not significantly melt the surrounding mantle lithosphere [Ellam et al., 1992]. Any modern signature of melt-depletion in the mantle lithosphere must represent earlier or subsequent processes. Because partial melting in the Archean occurred at higher temperatures than in the Proterozoic [e.g., Jordan, 1975], it is reasonable to infer that the pre-MCR midcontinent hosted more buoyant (but not necessarily seismically faster) mantle residuum in the Superior province (north) than in the Proterozoic terranes to the south. If this pattern is present and preserved, then it can be concluded that rift-related magmatism did not further deplete mantle lithosphere and that a thermal plume was not the primary cause of extension.

To better understand the origin and evolution of the MCR, we construct a 3-D density model of the midcontinent lithosphere, which highlights: (1) the spatial extent and magnitude of rift-related melt depletion, (2) how the volume of high-density mafic crust varies along strike and with depth, and (3) the response of recently extended and intruded crust to subsequent contraction. The first criterion can be used to discriminate between active and passive rifting in the MCR, which in turn determines whether there need be a significant asthenospheric driver for intracontinental rifting. The second can be used to explore the kinematics of extension. The last provides insight into the fate of intraplate rifts and their connection to future deformation. Finally, the development of a technique to reconcile seismic velocity, gravity, topography, and heat flow data is an important step in understanding the thermal and chemical structure of the crust and upper mantle in continental interiors.

### 3. Initial Density Model

Following Levandowski et al. [2014], an initial 3-D density model of the crust and upper mantle to 150 km depth is derived from the vertically polarized seismic shear-wave velocity ( $v_{sv}$ ) and crustal thickness model presented by Shen et al. [2013b]. This approach, detailed below, was largely successful in the western United States [Levandowski et al., 2014], where densities estimated from similarly derived seismic velocity and crustal thickness models [Shen et al., 2013a] generally reproduced gravity (to within  $\sim 30$  mGal, L1 norm) and flexurally modulated topography (to within 500 meters in 85% of locations).

This initial 3-D density model is based on empirical scaling relationships between seismic velocity and density. In the crust, compositional variations and thermal variations are modeled jointly. In the mantle, however, the initial density model is derived assuming that seismic velocity variations arise only from temperature

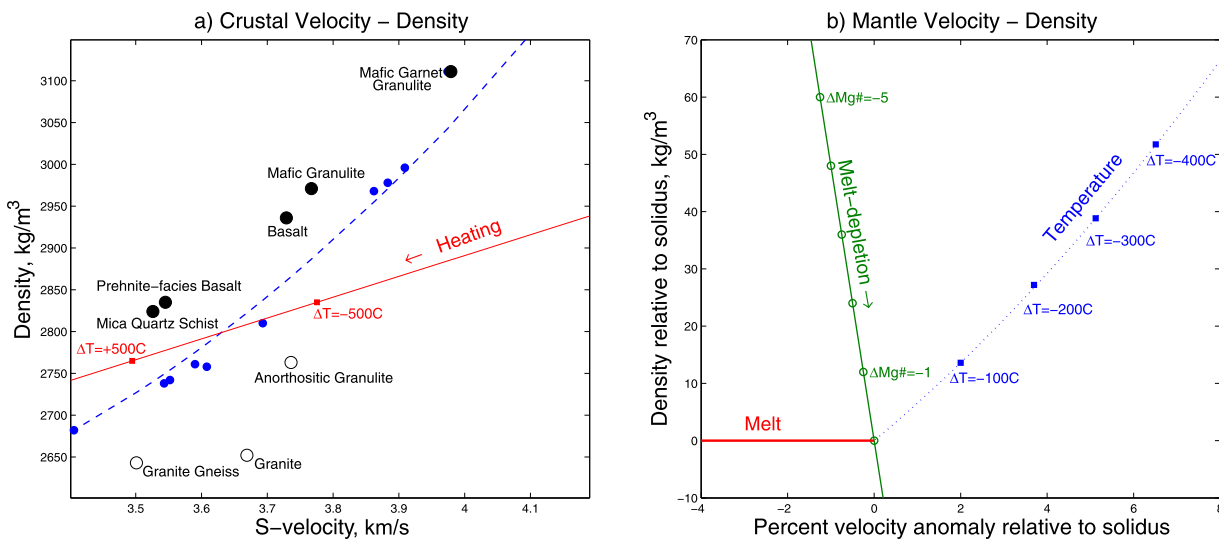


**Figure 2.** Velocity-density relationships. (a) Crust: Empirical velocity-density data for various crustal lithologies [Christensen, 1996; Brocher, 2005] and polynomial regression through them (equation (1), blue line). Lower velocity sediments and higher velocity lithologies such as eclogite, dunite, and pyroxenite are used in the regression but plot outside the bounds of this figure. Notable outliers are labeled; other data points are unlabeled open circles. Thermal trend shown in red is derived assuming constant  $v_p/v_s = 1.78$ ,  $\partial v_p/\partial T = 0.5$  m/s per °C, coefficient of thermal expansion of  $2.5 \times 10^{-5}$  per °C, reference velocity of 3.65 km/s and reference density = 2800 kg/m<sup>3</sup> [Christensen and Mooney, 1995]. (b) Mantle: Thermal  $\partial \rho/\partial v_s$  at a depth of 100 km and 1 cm grainsize (equation (4)) in blue. Below the solidus, decreasing velocity most likely reflects increasing melt content, which has negligible effect on density [Hammond and Humphreys, 2000]. The trend for increasing melt depletion, represented in terms of change in Mg-content, is shown in green [Schutt and Lesher, 2010].

variations. Before considering this initial, seismically derived density model, however, it is important to understand the sensitivities and shortcomings of the crustal and mantle scaling relationships.

### 3.1. Crustal Density

The initial model of crustal density is estimated from a regression of empirical density and velocity data of nonvolcanic, polymimetic rocks [Christensen, 1996] and sediments [Brocher, 2005], which is sensitive to composition but independent of pressure and temperature:

$$\rho = -15.84v_s^5 + 209.13v_s^4 - 961.94v_s^3 + 1863.36v_s^2 - 1163.00v_s + 2153.06 \quad (1)$$

This relationship is well suited to intermediate compositions but overestimates the density of felsic rocks by up to ~100 kg/m<sup>3</sup> and underestimates the density of mafic material by ~80 kg/m<sup>3</sup> (Figure 2a).

The relationship between crustal density and velocity due to temperature variations (Figure 2a) differs from equation (1) [Behn and Kelemen, 2003; Levandowski et al., 2013]. Consider crustal material with a density of 2800 kg/m<sup>3</sup>,  $v_s$  of 3.6 km/s,  $v_p/v_s$  of 1.78, coefficient of thermal expansion of  $2.5 \times 10^{-5}$ /°C, and  $\partial v_p/\partial T$  of 0.5 m/s per °C [Christensen and Mooney, 1995]. A 100°C temperature increase lowers density by 7.25 kg/m<sup>3</sup> and S-velocity by ~0.03 km/s, whereas a similar velocity decrease due to composition is modeled (equation (1)) as a ~17.6 kg/m<sup>3</sup> density decrease. Increasing temperature leads to a density underestimate of ~0.1 kg/m<sup>3</sup> per °C; hot material is denser than velocity suggests, and cold material less dense.

After scaling crustal velocity to density using equation (1), a correction,  $\Delta\rho_T$ , is applied to the estimated density for departures,  $\Delta a(z)$ , from some reference crustal geotherm:

$$\Delta\rho_T(z) = 0.1 \Delta T(z) \quad (2)$$

We assume a 15°C/km reference geotherm,  $T_{ref}(z)$ , and estimate temperature departures from this geotherm based on observed surface heat flow,  $q$ :

$$\Delta T(z) = zq/\kappa - T_{ref}(z), \quad (3)$$

Conductivity,  $\kappa$ , is assumed to be uniformly 3 W/m°C. Since heat flow in the study area spans the narrow range of ~35 to 45 mW/m<sup>2</sup> [Blackwell and Richards, 2004], the effect of putative temperature variations on the crustal density is minimal. A more careful consideration of crustal temperature variations that accounts

for heat producing elements and variability in thermal conductivity may be warranted in other, more thermally heterogeneous regions [e.g., *Hasterok and Chapman*, 2007].

At high crustal temperatures not expected in the midcontinent, melt may be present. Melt lowers shear-wave velocity by some 7.9% per 1% of in situ, connected melt [Hammond and Humphreys, 2000], but density is nearly constant at the solidus. Consequently, the density of melt-bearing crust is much greater than predicted from seismic velocity and heat flow (equations (1–3)). To illustrate, the velocity of a region of crust with  $v_s$  3.7 km/s that undergoes 1% melting decreases to 3.4 km/s. Equation (1) estimates densities of 2842 kg/m<sup>3</sup> and 2680 kg/m<sup>3</sup> from these velocities, even though density does not change appreciably at the solidus. In this example 1% in situ melt has led to a 162 kg/m<sup>3</sup> underestimate of density. This discussion has been included for completeness, despite the fact that large variations in crustal temperature and partial melt are not likely in the north-central United States.

Radially anisotropic velocity would influence the density model. For example, dikes or steeply dipping foliated micas or faults allow vertically polarized shear waves to propagate more quickly than horizontally polarized waves ( $v_{SV} > v_{SH}$ , “negative radial anisotropy”). If one uses  $v_{SV}$  in such situations, the estimated density would likely exceed the true density in those areas. In the case of the MCR, postrifting contraction likely precludes horizontal fabrics, and active source profiles suggest that rift-bounding faults dip steeply, but layered mafic intrusions [e.g., *Serpa et al.*, 1984; *Behrendt et al.*, 1990] are one possible source of positive radial anisotropy and the low  $v_{SV}$  within the rift.

### 3.2. Mantle Density

Mantle densities and velocities also vary laterally as functions of temperature and composition. Our starting density model accounts for temperature variations, seismic anelasticity, and melt production, but we do not yet consider compositional variations.

For each of six common upper mantle minerals—Fo<sub>90</sub>, Fo<sub>92</sub>, orthoenstatite, ferrosillite, garnet, and spinel—we use (1) published estimates of the shear and bulk moduli and their pressure and temperature-derivatives [Bouhifd *et al.*, 1996; Hugh-Jones, 1997; Jackson *et al.*, 2003; Afonso *et al.*, 2005], (2) temperature-dependent thermal expansivities [Afonso *et al.*, 2005], and (3) a temperature-, pressure-, and seismic-period-dependent calculation of the dynamic compliance, or the Laplace transform of the creep function (using scripts provided by Faul and Jackson and Faul [2010]) to account for anelasticity. The representative period of surface waves increases with depth (from ~30 s at 50 km to 80 s, the longest period used by Shen *et al.*, at 150 km), so these velocity-density relationships are depth dependent both because of increasing pressure and increasing seismic period.

Fitting the velocity-temperature and density-temperature curves for bulk pyroxenitic composition (30% Fo<sub>90</sub> + 30% Fo<sub>92</sub> + 25% OPX + 10% CPX + 2.5% Gt + 2.5% Sp) yields a relationship between velocity and density deviations from the assumed solidus ( $v_s = 4.5$  km/s;  $\rho = 3200$  kg/m<sup>3</sup>). At a depth  $z$ , a velocity perturbation ( $\Delta v_s$  quantified as percent of 4.5 km/s) scales to a density perturbation as:

$$\Delta\rho = \Delta v_s \times \left( 7.3 - \frac{z}{100 \text{ km}} + \frac{\Delta v_s}{4} \right); \Delta v_s \leq 6\% \quad (4a)$$

$$\Delta\rho = \Delta v_s \times \left( 8.8 - \frac{z}{100 \text{ km}} - \frac{7(\Delta v_s - 6)}{40} \right); \Delta v_s \geq 6\% \quad (4b)$$

The variations in this scaling among realistic compositions of the upper mantle are minor. The density change of depleted (Mg-, OPX-, and Ol-rich) material that corresponds to a unit velocity change is 5% (i.e., ~0.03 kg/m<sup>3</sup>) greater. Fertile (Fe-, Gt-/Sp-, and CPX-rich) material is 5% less sensitive.

While the slope ( $\Delta\rho/\Delta v_s$ ) is relatively insensitive to composition, the y-intercept of a plot of density versus  $v_s$  is strongly controlled by compositional variations, the most important of which is likely to be differences between fertile (iron-, clinopyroxene-, and garnet/spinel-rich) and melt-depleted (magnesian and orthopyroxene-rich) mantle [e.g., *Jordan*, 1979; *Godey et al.*, 2004]. Hereafter, we will use Mg:Fe ratio as a proxy for melt-depletion, quantified in terms of Mg# = [Mg]/[Mg+Fe]. Empirical relations among Mg#, seismic velocity, and density [Lee, 2003; *Matsukage et al.*, 2005; *Schutt and Leshner*, 2010] suggest that a unit increase in Mg# corresponds to a 0.4–0.5% (13 kg/m<sup>3</sup>) decrease in density and a 0.25–0.45% (~0.015 km/s) increase in velocity (Figure 2b). Since the latter would be modeled as a 2 kg/m<sup>3</sup> increase in density, a unit increase in

Mg# leads to a density overestimate of  $15 \text{ kg/m}^3$  under the assumption that all velocity variations are thermal in origin (Figure 2b). Hence, the  $\pm 1.5\%$  mantle shear-wave velocity variations reported by *Shen et al.* [2013b] could arise from Mg# variations of  $\pm 4$ , though a  $100 \text{ kg/m}^3$  density difference would accompany such compositional heterogeneity.

#### 4. Observations and Predictions

The density model derived from seismic velocity and heat flow is interpolated on a Cartesian grid that extends  $\sim 200 \text{ km}$  beyond the seismic footprint, an effort to minimize edge effects. Results beyond the geographic bounds of the input velocity model are discarded. Interpolation is linear within the bounds of the input velocity model and nearest-neighbor past its edges. The model grid is separated into laterally varying layers. The crust, which varies from  $<40 \text{ km}$  to  $>50 \text{ km}$  thickness, is represented by 0–5 km (subsuming the sediment thickness variations in the region [*Frezon et al.*, 1988]), 5–15, 15–25, 35–45, and 45–55 km layers; this vertical spacing is arbitrary but is similar to the length scale of lithologic variations observed in some exposed mid and lower-crustal sections [*Holliger et al.*, 1993; *Goff et al.*, 1994; *Rudnick and Fountain*, 1995; *Weiss et al.*, 1999]. The mantle is divided into  $\sim 30 \text{ km}$  thick layers: 55–85, 85–120, and 120–150 km depth. Again, this spacing is arbitrary, but trials with an increased number of mantle layers did not produce demonstrably better feature recovery, and instead simply increased processing time. Densities derived from the seismic velocity model are interpolated onto this mesh, with each cell having a uniform density (Figure 3).

##### 4.1. Topography

This initial density model predicts local isostatic topography,  $E$  (following *Lachenbruch and Morgan* [1990]):

$$E = H - H_0; \quad H = \int_0^{z_a} \frac{\rho_a - \rho(z)}{\rho_a} dz. \quad (5)$$

$H_0$  is a correction term of 2.4 km to achieve isostatic equilibrium with an asthenospheric column (via mid-ocean ridges). The mantle below the base of the seismic models ( $z_a$ ) at 150 km depth is assumed to be laterally uniform, with a density ( $\rho_a$ ) of  $3200 \text{ kg/m}^3$ . While high velocity material likely extends to 200–250 km beneath the midcontinent [*van der Lee and Nolet*, 1997; *Frederiksen et al.*, 2013], this feature is broadly uniform, so it should not generate appreciable relief within our study area. Similarly, small lateral variations below 150 km depth will not generate a significant signal in the gravity field.

Lithospheric flexural strength modulates local buoyancy. Convolution of  $E$  with the flexural filter of the lithosphere,  $F$ , accounts for flexural smoothing and results in the smoothed surface elevation field,  $\varepsilon$ , predicted from the lithospheric density estimate:

$$\varepsilon_{predicted} = E * F. \quad (6)$$

$F$  is a system of zero-order Kelvin-Bessel functions [*Watts*, 2001] based on a uniform elastic thickness throughout the study region, which is varied from 40 to 80 km [*Kirby and Swain*, 2009; *Watts*, 2012]. Similarly, the convolution of observed surface elevations with  $F$  produces a smoothed elevation field,  $\varepsilon_{observed}$ . For the estimated lithospheric density structure to be plausible,  $\varepsilon_{predicted}$  must match  $\varepsilon_{observed}$  within some tolerance.

##### 4.2. Gravity

The density structure should also reproduce observed gravity variations. To calculate a predicted gravity field, the mean density in each layer of the model is removed in order to diminish edge effects. The sums of the vertical component of the attraction of each cell on each surface node then represent the predicted gravity field, with its mean removed. This 2-D grid of gravity variations is compared to free air gravity anomalies from the National Geophysical Data Center [*Dater et al.*, 1999] interpolated to the same grid (Figure 1a).

##### 4.3. Gravity and Topography Residuals

Neither the gravity nor topography predicted by the initial density model (Figures 4a and 4c) matches the observations (Figures 1a and 1b). The residual gravity ( $G_r$ ) and topography ( $H_r$ ) highlight this failure (Figures 4b and 4d):

$$G_r = G_{observed} - G_{predicted}; \quad H_r = \varepsilon_{predicted} - \varepsilon_{observed} \quad (7)$$

Polarities are such that positive values imply the need for greater density in each.

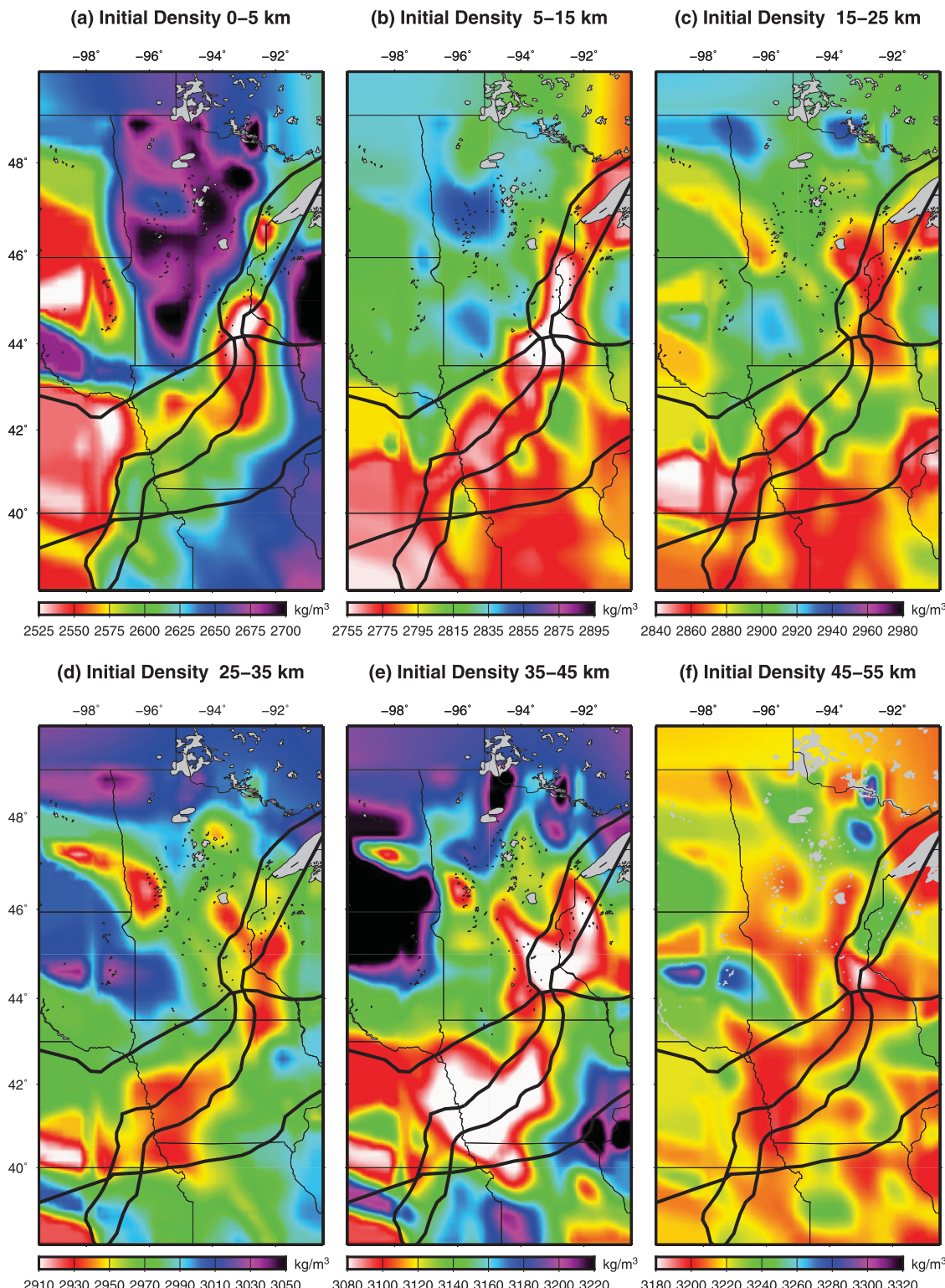


**Figure 3.** Densities estimated from seismic velocity and crustal thickness. The MCR is predicted to have buoyant crust rather than the dense material inferred from gravity (Figure 1a).

More than 1 km of relief is predicted within the nearly flat study area, and the rift is predicted to be a regional gravity low; this initial model is clearly invalid. From this starting point, we develop a technique to adjust the seismically derived starting model to reconcile the gravity and topography residuals. Our goal is

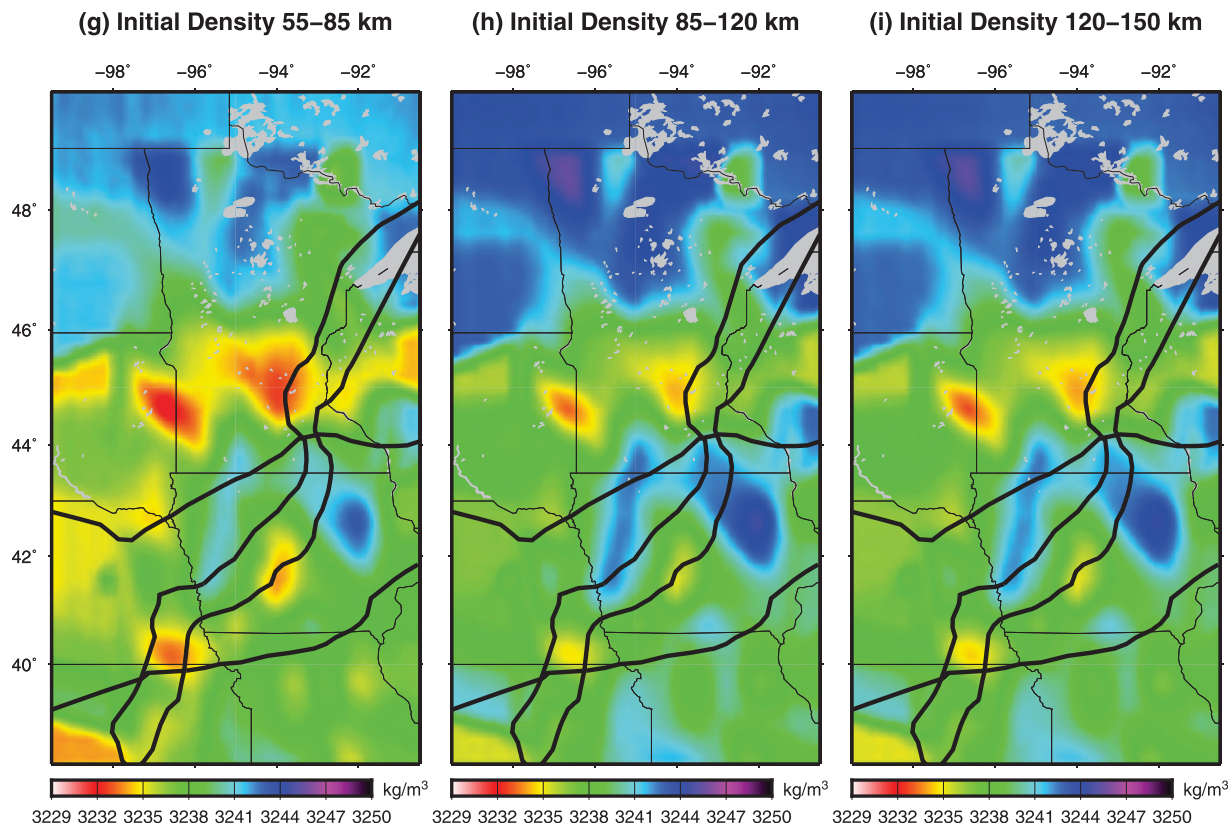


Figure 3. (continued)

not only to produce a plausible model of the density of the MCR and surroundings but also to illuminate possible causes of the observed variations in density and velocity.

## 5. Density Refinement Algorithm

Given the failure of the initial density model to recover the regional gravity field and surface elevation (Figures 4b and 4d), this initial model must be refined. The residual gravity and topography data sets constitute a basis because of their different and linear sensitivities to 3-D density structure. Surface elevation results from density integrated over depth (equation (2)), convolved with the flexural filter (equation (3)); gravity decays with distance to the mass squared. As such, the gravity and topography are suited for a linear inversion [e.g., Sheehan and Solomon, 1991]. Nevertheless, the physical origin of the present challenge is the nearly random scatter of possible densities about a given velocity. There exists a range of plausible adjustments to the 3-D density model that will reproduce both within uncertainty or to a prescribed tolerance. To the extent possible, sampling of this distribution ought not be biased by selected smoothing and damping parameters. Finally, we seek to limit the biases introduced by the specific starting model (i.e., by the seismic velocity and crustal thickness model). For these reasons, we favor an approach that embraces the non-uniqueness of gravity and of topography, requires minimal parameterization, and departs from the starting model to the extent allowed (not the minimum required) by the data.

The density model from the velocities of *Shen et al.* [2013b] and equations (1–3) will now be viewed as a starting model, and its attendant gravity and topography residuals “inverted” for additional density variations that recover both fields. The term inversion is used loosely, as the algorithm comprises iterative, random-walk Monte Carlo simulations and as such repeatedly solves the forward problem. Comparison of the seismically derived starting model and the final density distributions aids in understanding the thermal and compositional sources of density variations.

For a series of 3000 simulations, the density model derived from seismic velocity and heat flow is interpolated on a grid of 30–60 km lateral dimension, 0.5–1 times the Transportable Array station spacing. The width varies

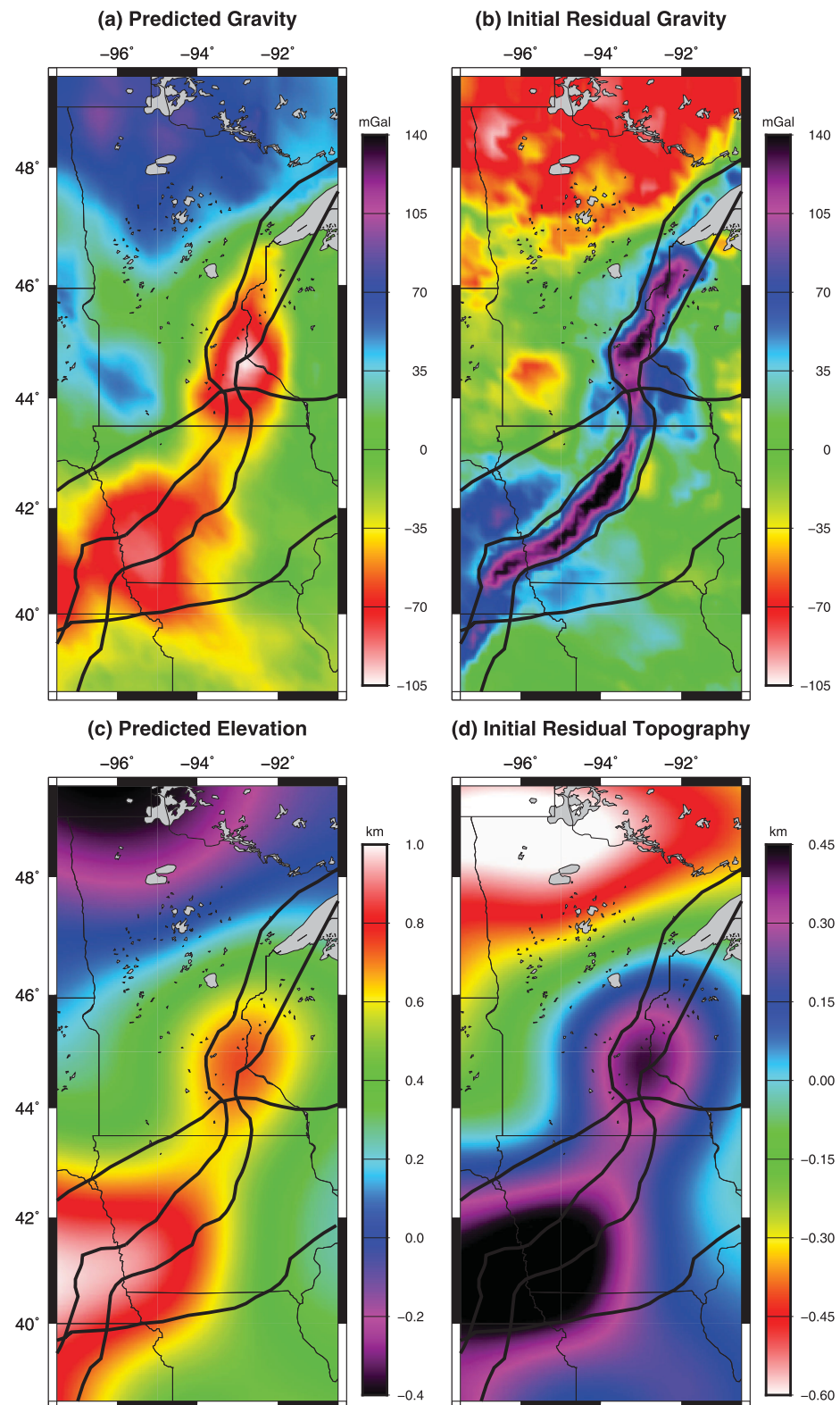


**Figure 4.** Predicted gravity and topography from the initial density model (Figure 3), and residuals (i.e., compared to Figures 1a and 1b). (a) Predicted gravity variations (i.e., the mean has been removed). (b) Residual gravity, or observed minus predicted variations. Polarity is such that positive values imply a need for greater density. (c) Predicted flexurally modulated surface elevation. (d) Residual topography, or predicted minus observed elevation. Polarity is such that positive values imply a need for greater density.

randomly with each new simulation in an effort to mitigate biases imposed by the geometry of the starting model. The predicted Free Air gravity variations and flexurally smoothed topography are calculated (equations (5) and (6)) at each surface grid point. These predictions are compared (equation 7) to observations interpolated at the same grid point to calculate the residual gravity and topography to be modeled.

Simulations proceed by selecting a single grid point within the study area at pseudo-random, with the likelihood of each point's selection weighted by the current magnitude of its residuals. Two cells beneath this point are then chosen at random (e.g., in the 10–20 km and the 55–85 km layers), and the density in each cell takes a random walk about its current value (with length sampled from a uniform distribution  $\pm 75 \text{ kg/m}^3$  in the crust and  $\pm 25 \text{ kg/m}^3$  in the mantle). The walk is further limited to stay within  $150 \text{ kg/m}^3$  of the starting model in the crust (mimicking the maximum misfit of the crustal velocity-density regression) and  $\pm 50 \text{ kg/m}^3$  in the mantle, a largely arbitrary value. We calculate the changes in gravity and topography and the attendant model-wide weighted variance,  $V$ , for each cell-walk trial:

$$V = \sum (\text{var(}(\text{Gravity Residuals}/W)\text{)} + C) \times (\text{var(}(\text{Topography Residuals})\text{)} + C). \quad (8)$$

Here  $W$  is an adaptive relative weight that depends on the current state of the model:

$$W = 30 \times (\# \text{Topography beyond tolerance} + 1) / (\# \text{Gravity beyond tolerance} + 1). \quad (9)$$

$C$  is a constant greater than 0 that forces convergence (e.g., if all topography were perfectly reproduced, without  $C > 0$  gravity would have no effect and vice versa). The value of  $C$  has little impact on results; we arbitrarily use  $C = 100$ . The cell-walk trial with minimum  $V$  is accepted, regardless of whether the variance is reduced or increased. As in other random-walk or simulated annealing algorithms, allowing for increases in variance helps to avoid stability wells, speeds model convergence, and mitigates the effects of erroneous starting models. The residuals are updated accordingly, a new grid point is chosen at random, and a new iteration begins. The number of cell-walk trials—initially two—examined in a given iteration increases slowly through the simulation to speed convergence.

The simulation continues until the 3-D density model reproduces gravity and topography at all grid points to within an arbitrary threshold (here 50 meters and 5 mGal), and a new simulation begins: creating a new mesh of points, interpolating the seismically estimated density, calculating gravity and topography residuals, and finding a new 3-D density model that reproduces gravity and topography. In general, the L1 norm, or average absolute value, of the gravity residuals is less than 2 mGal and that of the topography residuals is less than 20 meters.

The results we discuss below are all acceptable models from a suite of 3000 simulations (i.e., 3000 3-D density models) and are binned into 30x30 blocks. This posterior distribution is meant to represent the values allowed by the data, not an optimal solution. Unless otherwise noted, the values presented are the mean within each cell across the 3000 simulations. Because of the large number of simulations and because the meaningful quantity is the mean across the suite of simulations, uncertainties (i.e., standard deviations of the mean) are  $< 1 \text{ kg/m}^3$  and not discussed further. For the  $\sim 900 \text{ km} \times 1400 \text{ km}$  study area, each simulation takes  $\sim 30$  s, though computational cost increases in proportion to the square of the surface area of the region in question and/or the grid spacing.

## 6. Synthetic Resolution and Recovery Tests

Before examining real data, it is crucial to understand the resolution and shortcomings of the algorithm, particularly whether it is capable of resolving the structures that have been proposed in the midcontinent. Specifically, it is important to understand how well this approach can resolve the true density structure (as manifest in gravity and topography) despite the fact that the input seismic velocity model does not mirror the subsurface density. That is, does inverting the residual gravity and topography lead to the proper corrections to the initial density model?

Each of the tests below begins from a uniform starting model to which  $\pm 30 \text{ kg/m}^3$  random noise is added. In each case, an additional density anomaly is prescribed, and the predicted gravity and topography variations from the density anomaly and the random noise constitute the input residuals (i.e., relative to a uniform starting model) that are then inverted.

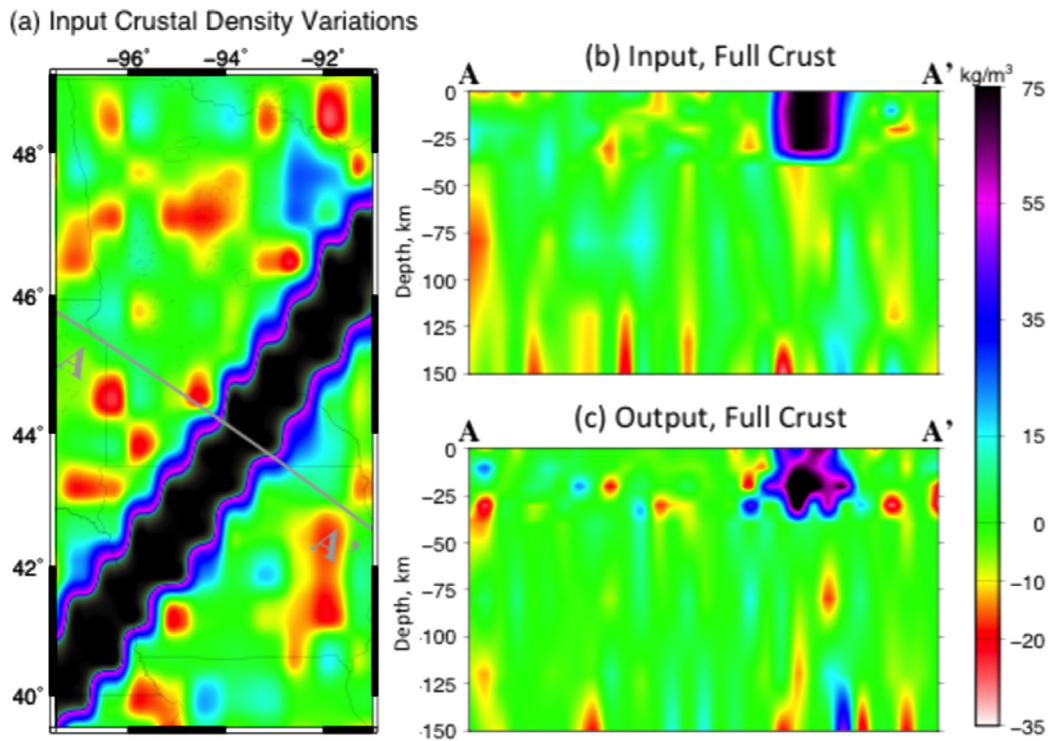


**Figure 5.** Feature recovery test of a crustal scale set of mafic intrusions. (a) Map view of input density anomaly relative to an arbitrary estimate from seismic velocity. Cross sections in Figures 5–7 are from A–A'. (b) Cross-section of input density anomaly relative to seismically derived estimate. (c) Output density adjustment.

In a set of supporting information Figures S1–S3, we gauge the relative sensitivity of the final model to velocity, gravity, and topography by creating density models using a 1-D starting model and then refining this to reproduce gravity and topography; using a 1-D model and refining this to reproduce gravity alone (i.e., ignoring both velocity and topography); and using the 3-D starting model (Figure 3) and then refining this to reproduce gravity alone (i.e., considering gravity and velocity but not topography).

### 6.1. Rift Spanning the Crust

The simplest feature that this algorithm should recover is a set of mafic intrusions that runs from the Moho to near the surface without affecting the mantle. Since mafic material is generally  $\sim 75 \text{ kg/m}^3$  denser than the initial (seismically derived) model would estimate (Figure 2a), a  $+75 \text{ kg/m}^3$  anomaly is added from 0 to 40 km depth to a region  $\sim 150$  km wide that runs SW–NE across the study area, similar to the real MCR. Calculating and then inverting the gravity and topography residuals created by this body recovers a feature (Figure 5) that is not smeared laterally or vertically but has a somewhat smaller density anomaly than the input ( $\sim 60 \text{ kg/m}^3$  versus  $75 \text{ kg/m}^3$ ). Note that the random noise that was added is not recovered.

### 6.2. Lower Crustal Intrusions

Some refraction profiles suggest that changes in P-velocity within the MCR are more pronounced in the lower crust than the upper 20 km. To mimic this feature, a  $+75 \text{ kg/m}^3$  anomaly is added from 20 to 40 km (Figure 6). In recovering this feature, the vertical resolution of this algorithm is imperfect, as it smears the input anomaly upward some 10 km and reduces its magnitude by  $\sim 50\%$ . Additionally, some of the high-density material is smeared downward into the upper mantle (mean density is  $\sim 10 \text{ kg/m}^3$  in the 40–55 and 55–85 km layers). This potential for vertical smearing should be recalled when considering the features recovered from real data, below.

### 6.3. Rifting Crust Overlying Depleted Mantle

A demonstration that the vertical resolution of the inversion algorithm is sufficient to separate mafic crust from underlying depleted mantle is of paramount importance to determining whether or not the mantle

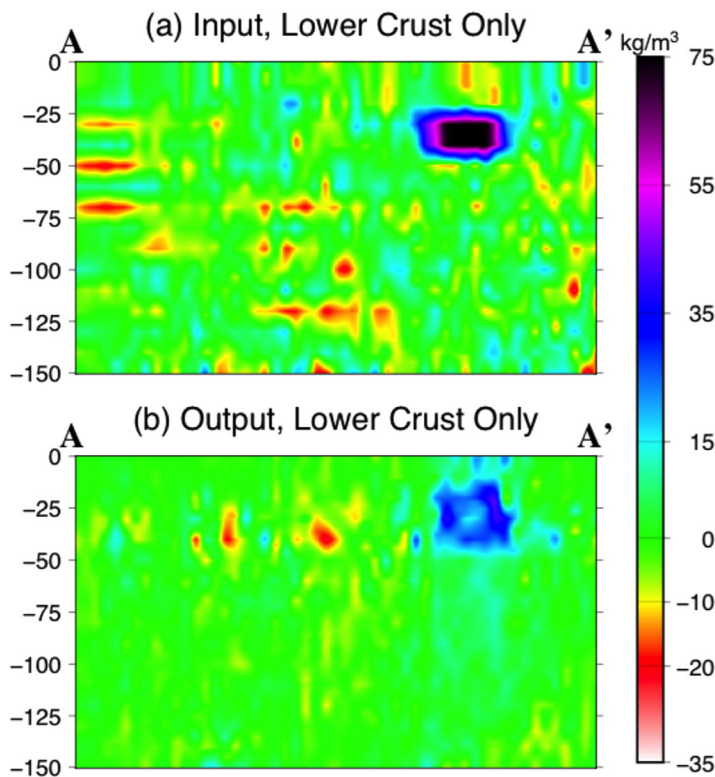


**Figure 6.** Feature recovery test of lower crustal intrusions. The input is the same in plan view as Figure 5a.

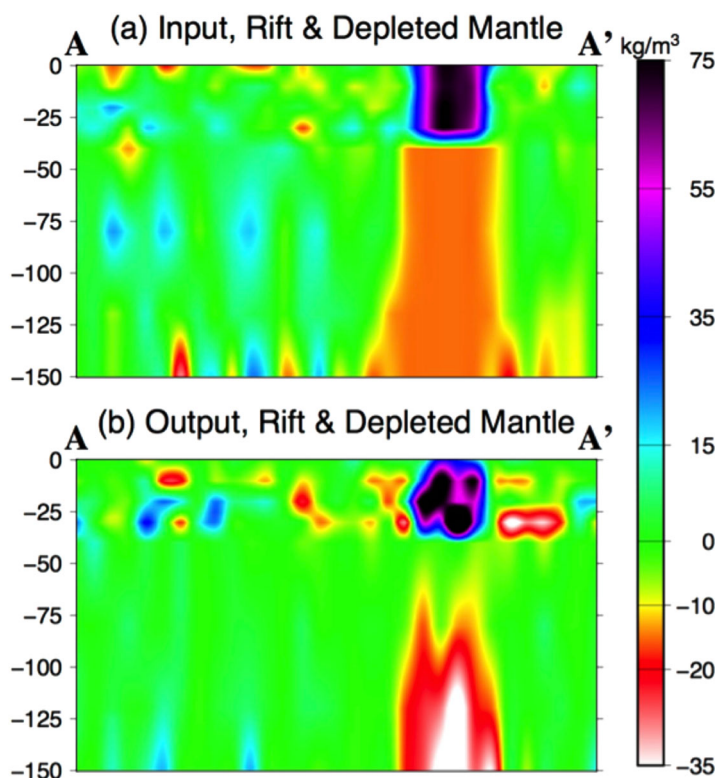


**Figure 7.** Feature recovery test of full crustal rift overlying depleted mantle.

beneath the rift was depleted during volcanism. Since mafic material has a greater density than predicted by seismic velocity, the seismically derived starting model should underpredict gravity. Simultaneously, melt-depletion of the underlying mantle could increase its buoyancy, offsetting the load of the mafic crust and decreasing or eliminating the topographic residual. Such a pattern of mafic crust overlying depleted mantle is tested with a  $+75 \text{ kg/m}^3$  body from 0 to 40 km that overlies a  $-25 \text{ kg/m}^3$  mantle from 40 to 150 km depth. Despite the fact that mantle buoyancy offsets crustal density, the algorithm is able to recover both structures to some degree (Figure 7). The primary shortcoming is vertical resolution in the mantle layers. Rather than  $-25 \text{ kg/m}^3$ , the uppermost mantle density is estimated as  $-10 \text{ kg/m}^3$ , and the density of the lowermost mantle is correspondingly  $-40 \text{ kg/m}^3$ . This shortcoming is another manifestation of the vertical smearing of lower crustal density anomalies into the uppermost mantle.

## 7. Density Model for the Midcontinent Rift

As discussed above, the seismic velocity model presented by *Shen et al. [2013b]* is used to estimate the initial density of the crust and upper mantle (using equations (1) and (2) in the crust and assuming an isochemical mantle: equation (4)), but this estimate does not faithfully reproduce gravity and topography (Figures 4b and 4d). Using the algorithm developed here, the seismically derived density estimate is refined, allowing for deviations from the uniform scaling of crustal velocity to density.

We also relax the assumption that mantle velocity variations are purely thermal in origin. By allowing deviations from empirical scaling of crustal velocity to density by an amount justified by observations of scatter in velocity-density relations, our approach prevents crustal density anomalies (e.g., mafic lithologies in the crust) from being mapped into the mantle. Further, the deviation of density from the seismically derived estimate may illuminate lithologic variations that are obscured in velocity models. Mafic lithologies are denser than the regression (equation 1) of density onto velocity for a suite of rock types would suggest. Variations in mantle density that are not mirrored in seismic velocity plausibly represent variable melt-depletion but are unlikely to arise from temperature variations, since these should manifest in seismic velocity.

Crustal density outside the MCR is well approximated by velocity alone (Figure 8a), whereas the MCR crust is some  $50 - 100 \text{ kg/m}^3$  denser than its  $v_{sv}$  suggests. The MCR is dense compared to its surroundings at all crustal depths, but the density contrast is most prevalent in the mid-lower crust (Figures 9b, 9c, and 10). Thick crust (locally  $>50 \text{ km}$ ) within the rift and on its flanks [Shen et al., 2013b] has dichotomous density from 35 to 55 km depth (Figures 9e and 9f). Relative to the mantle material present elsewhere at this depth range, the crust beneath the rift-flanks is predictably buoyant. The crust beneath the rift, however, is even denser than surrounding mantle material. Despite the imperfect vertical resolution of the algorithm, the magnitude of the recovered density anomaly beneath the rift is too great to result solely from vertical smearing (though the high density in the upper mantle, 55–85 km, beneath the rift (Figure 9g) may well be an artifact).

Mantle density broadly decreases with increasing age from the Yavapai terrane (Proterozoic) in the south to the Superior craton (Archean) in the north (Figures 9g–9i). This gradient results not from the starting model but from the adjustments required to reconcile gravity and topography: the mantle in the Superior Province is some  $10 \text{ kg/m}^3$  less dense than suggested by seismic velocity, and the Mazatzal Province some  $10 \text{ kg/m}^3$  denser (Figure 8b). Considering the feature recovery test shown in Figure 6, the high densities beneath the rift in the 55–85 km layer may be an artifact of the inversion and instead reside in the lower crust. Otherwise, there is nothing anomalous about the density beneath or near the MCR relative to the rest of the region, except perhaps in the northernmost portion of the study area where the mantle is  $5-10 \text{ kg/m}^3$  less dense than its surroundings from 120 to 150 km depth.

From a methodological perspective, the algorithm is acceptably fast and capable of generating density models that closely reproduce gravity and topography variations. The full set of 3000 simulations (e.g., Figure 11) was conducted in approximately 12 h on a MacBook Pro with 2.4 GHz processor and 4GB, 1333 MHz memory module. The L1 norms, or average absolute values, of the accepted misfits from each of the 3000 simulations are less than 2 mGal and 20 meters. This efficacy in the face of the MCR's discordant topography, gravity, heat flow, and seismic velocity suggests that this approach is suited to developing high spatial-resolution density models in even the most challenging settings.

## 8. Discussion

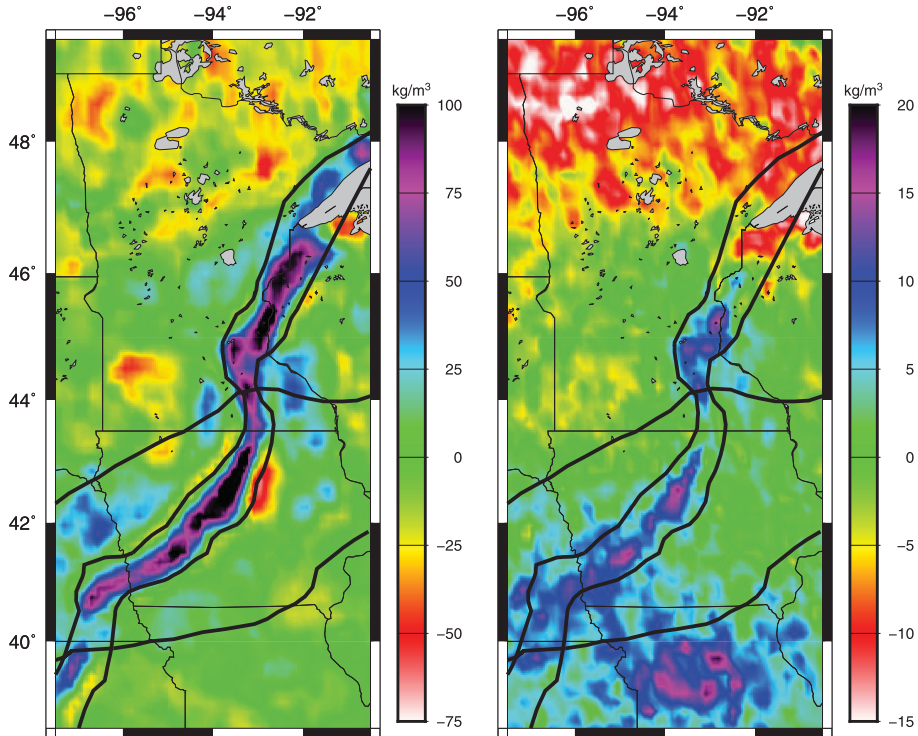
The geologic structure of the MCR is not recovered from density models that rely only on the shear-wave velocity of the crust and upper mantle. Consideration of gravity and topography as well, however, results in a more realistic depiction of the structure of the crust, the composition of the mantle lithosphere, and the interaction among asthenosphere, mantle lithosphere, and crust during this example of intracontinental deformation.

### 8.1. Recovery of Known Features in the Midupper Crust

In the middle and upper crust, the density model reveals the following features, none of which is unexpected:

1. dense crust in the iron ore-bearing rocks of northern Minnesota in the upper 15 km,
2. a large lateral contrast in density between rift-flank sediments and the mixed volcanic, intrusive, and sedimentary rocks of the MCR in the uppermost 5 km,
3. relatively uniform middle crustal density from 15 to 35 km throughout the region, except the MCR, which is  $\sim 50-100 \text{ kg/m}^3$  denser, and
4. a diminished density anomaly beneath the rift from 35 to 45 km.

(a) Average Density Change 0–55 km      (b) Average Density Change 55–150 km



(c) Final Residual Gravity

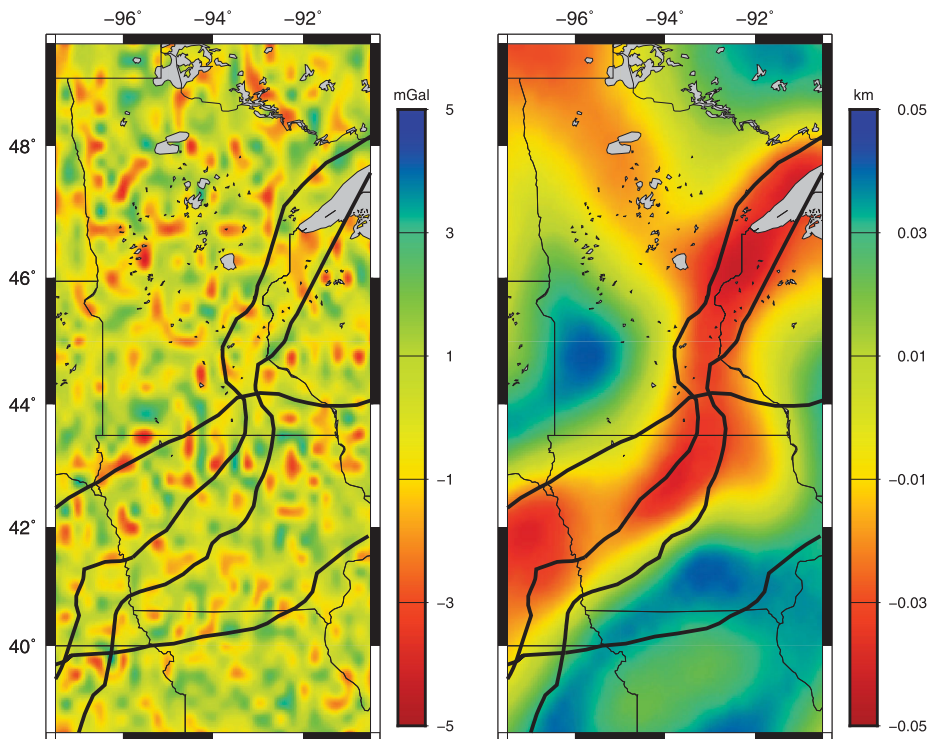


**Figure 8.** Average changes to the initial model and final residuals. (a) Average change to seismically estimated density from 0 to 55 km over 3000 simulations. The mafic crust of the MCR is up to  $100 \text{ kg/m}^3$  denser than modeled by equation (1). (b) Average change from 55 to 150 km. The mantle of the Superior province is more buoyant than calculated from equation (4). (c) Gravity residual after one of 3000 simulations. Node spacing for this particular simulation is 40 km. (d) Topography residual after one of 3000 simulations.

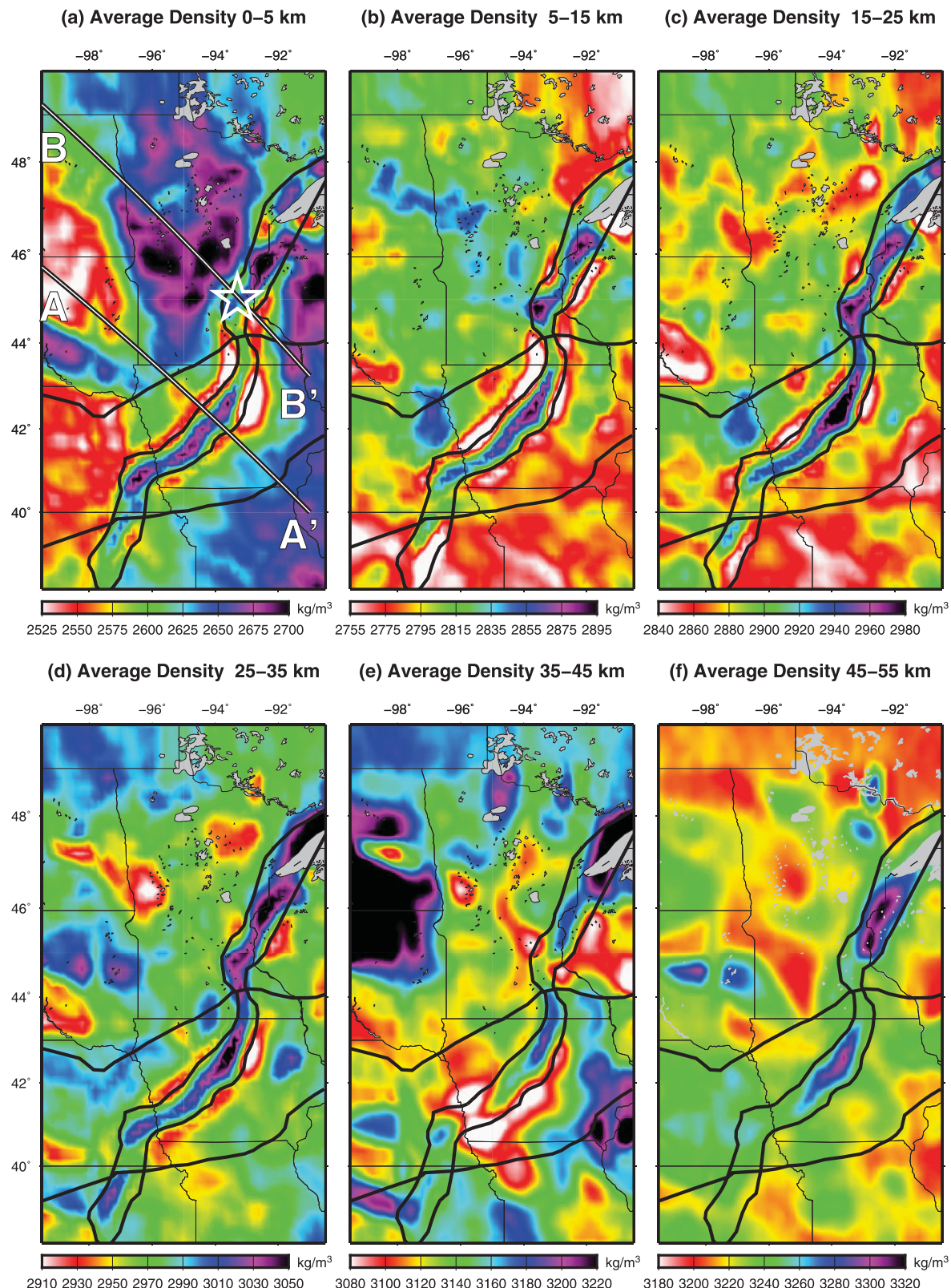


**Figure 9.** Average final density at the depths shown. The Midcontinent Rift is prevalent from 5 to 35 and 45 to 55 km depth, but it has no signal in lower mantle density. Instead, there is a broad N-S gradient in density from 85 to 120 km depth. Cross sections A-A' and B-B' on Figure 9a are shown in Figure 10. The 1-D profiles shown in Figure 11 are from beneath Minneapolis, marked with the white star on Figure 9a.

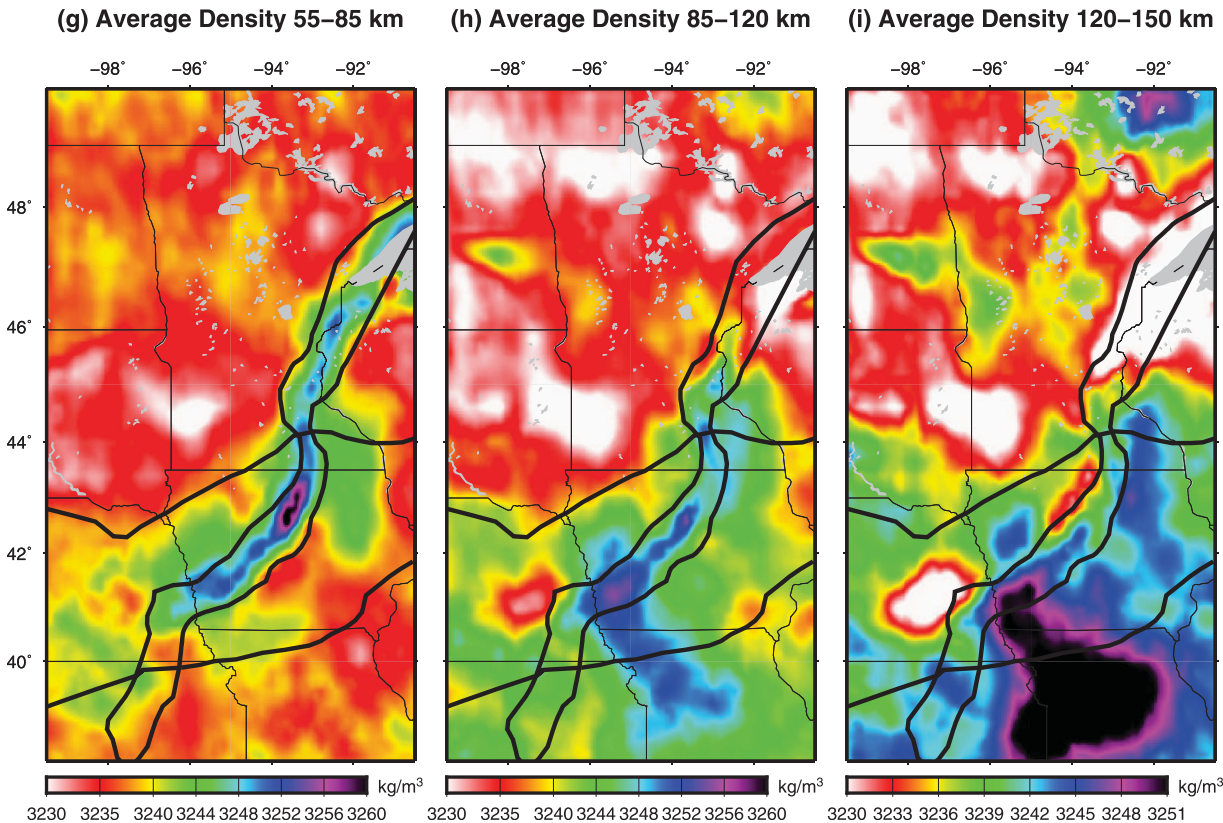


**Figure 9.** (continued)

The first three features are well known and previously documented. The fourth can be understood by considering that the zone from 30 to 40 km outside of the rift represents Archean and Proterozoic lower crust, where mafic rocks are thought to generally predominate [e.g., Rudnick and Fountain, 1995]. Hence, addition of mafic material beneath the MCR would not lead to anomalous density at these depths.

### 8.2. Eclogitic Lowermost Crust Beneath the MCR: The Result of Contraction

The keys to understanding the kinematics and evolution of rifting lie in observations below 35 km. First, the 35–55 km region is mostly upper mantle in the majority of the study area but mostly crust beneath and in places adjacent to the MCR [Shen *et al.*, 2013b]; this thickened crust has been previously attributed to a period of compression [e.g., Behrendt *et al.*, 1990; Cannon, 1994] that followed rifting by less than 20 Ma [Bornhorst *et al.*, 1988; Cannon and Hinze, 1992]. On the flanks of the rift this crustal material is now the most buoyant in the region in this depth range (Figures 8 and 9), but the lowermost crust beneath the rift is even denser than what is mantle elsewhere at these depths.

The presence of eclogite is a potential explanation for the exceptionally dense material in the lowermost crust beneath the MCR and is consistent with the low impedance contrast across the Moho in the northern MCR reported by Shen *et al.* [2013b]. We envision a scenario in which thickening of the rifted crust advected material downward, either under pure shear or because of the isostatic response to thrust loading. As thermal relaxation of the rift reduced the temperature in the lower crust, mafic material would have undergone retrograde, isobaric metamorphism, allowing it to enter eclogite facies below roughly  $900^\circ\text{C}$  [Green and Ringwood, 1967a]. Indeed, the temperature predicted from a surface heat flow of  $45 \text{ mW}/\text{m}^2$  is  $\sim 500^\circ\text{C}$  at 1.5 GPa, or  $\sim 50$  km depth [e.g., Hasterok and Chapman, 2007], well into the eclogite stability field. In contrast to the hypothesized occurrence of eclogite beneath the MCR, the rift flanks host low-density material, especially from 35 to 45 depth km, possibly representing crust that was not intruded during MCR extension but was thickened during postrift contraction. Because of the modern high flexural rigidity of the region [Kirby and

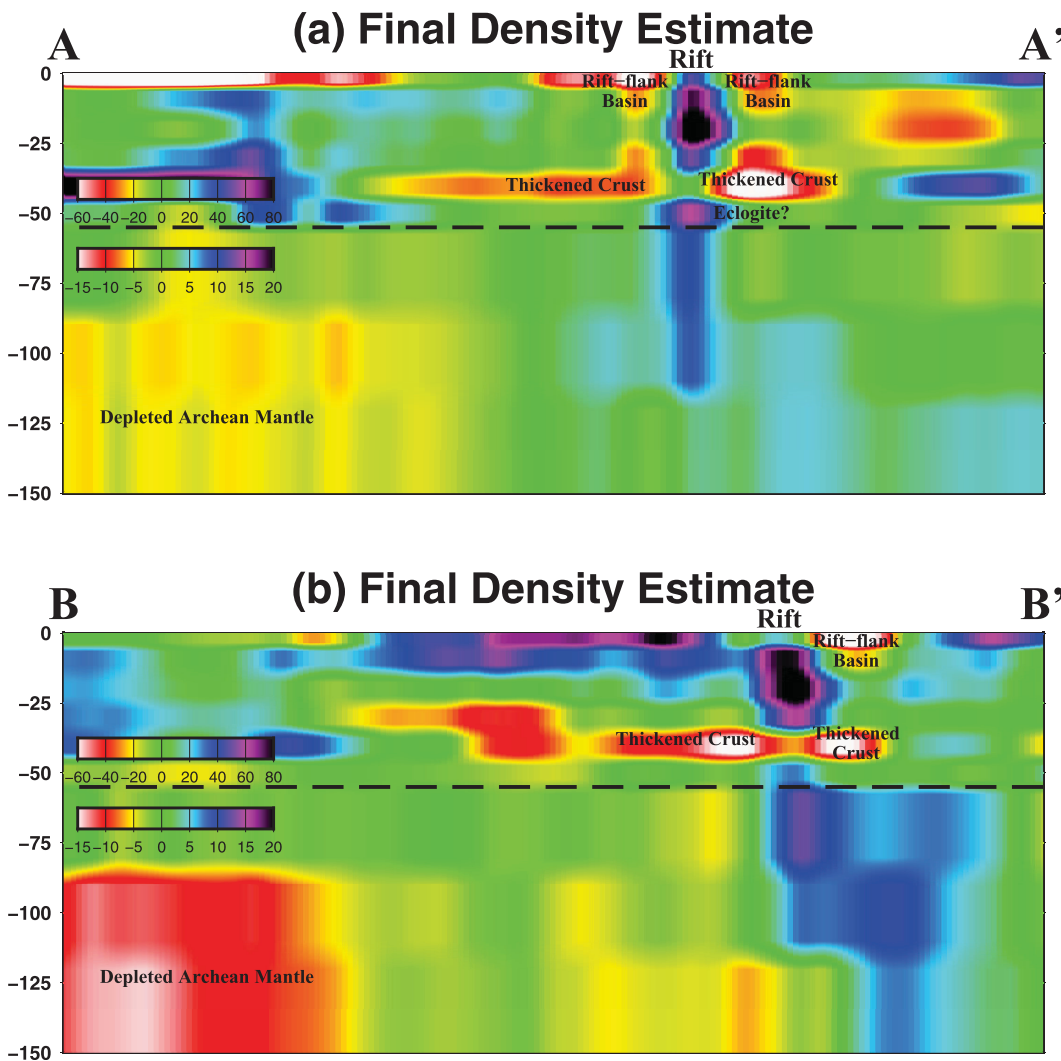


**Figure 10.** Cross sections through final density model as shown in Figure 9a. Densities are displayed as relative to the mean across the study area at each depth.

Swain, 2009; Watts, 2012], this buoyant crust on the rift flanks contributes to the topographic support of the dense material beneath the MCR.

### 8.3. No Mantle Depletion During Rifting: Evidence for Passive Rifting

The second key observation regarding the evolution of rifting bears not on the legacy of extension but on its origin: whether the MCR formed in response to far-field stress or forces exerted by the primitive mantle material that was beneath it. One prediction of the active-rifting model in previously unfractured lithosphere is that the responsible plume would heat the lithosphere until it is sufficiently weak to fail under its increased gravitational potential energy [Kent *et al.*, 1992]. During this period of tens of Myr, the plume would preferentially melt iron-rich fractions of the mantle lithosphere, leaving behind a depleted and chemically buoyant residue [White and McKenzie, 1989]. Unless such a depleted zone is only present below 150 km depth, this prediction is at odds with the density model of the MCR and surroundings, in which the density of the mantle beneath the MCR is not different from its surroundings (Figures 7b, 8g–8i, and 9). This observation suggests that rift-related melting does not control the modern state of the mantle lithosphere, consistent with geochemical evidence that the mantle lithosphere was not a volumetrically important contributor to magma production.

Instead, the dominant pattern in mantle density is a north-to-south increase. From density alone, one might suspect that this gradient reflects decreasing temperature, but seismic velocity does not capture this signal. An internally consistent explanation for seismic velocity and mantle density is that the south to north density

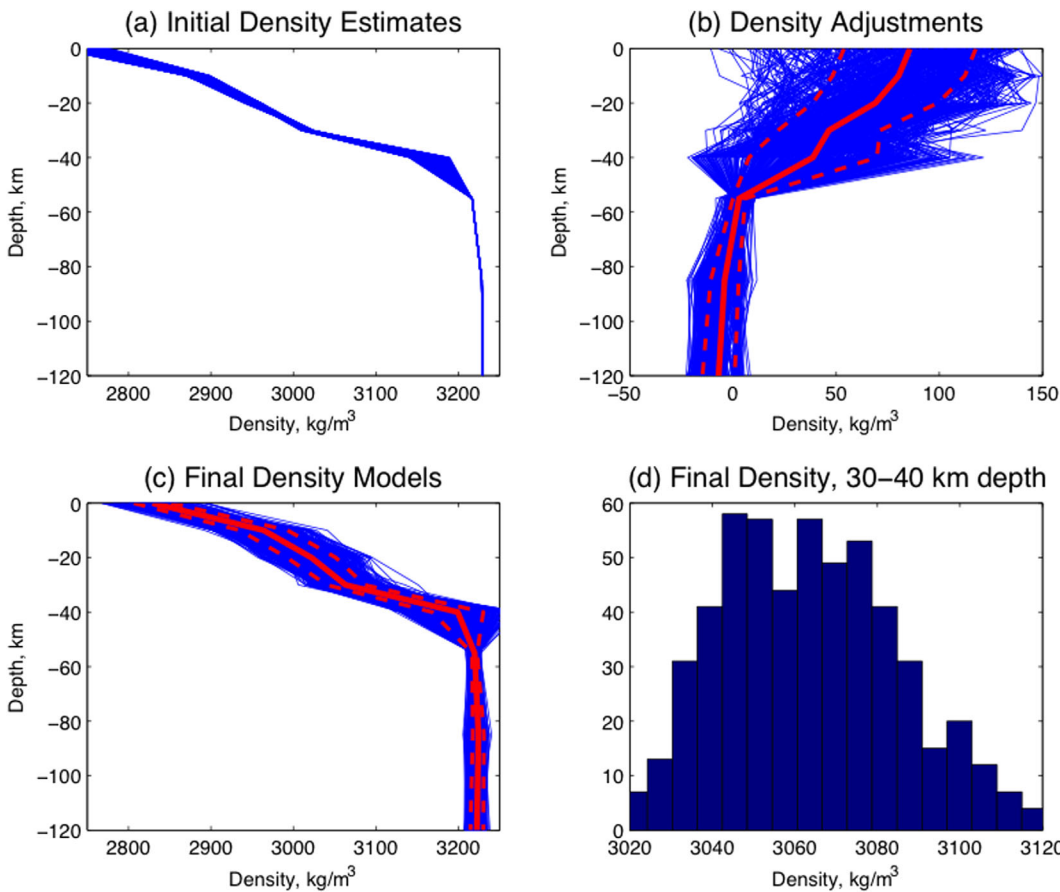


**Figure 11.** Example distributions within 20 km of Minneapolis (star in Figure 9a), 2775 total models shown. (a) Prior distribution of densities. (b) Distribution of 2775 1-D adjustments to (a). (c) Distribution of final densities. The mean values at each depth are shown by the solid red line, and the dashed lines mark the  $\pm 1\sigma$  bounds on the density at that depth. Average  $1\sigma$  uncertainty for a given simulation is  $22 \text{ kg/m}^3$  in the crust and  $5 \text{ kg/m}^3$  in the mantle. Nevertheless, the meaningful quantity is the average density across all acceptable models. Because of the large number of simulations the uncertainty of that mean is less than  $1 \text{ kg/m}^3$  at all depths. (d) Histogram of the posterior distribution in the 30–40 km layer.

decrease records increasing mantle iron-depletion with age as is reported globally, inherited from the time of crustal differentiation [Jordan, 1978, 1979; Boyd, 1989]. As discussed above, a 1% increase in Mg-content corresponds to a density decrease of  $\sim 13 \text{ kg/m}^3$  and an increase in seismic velocity of  $\sim 0.25\%$ . Hence, the Archean Superior region may have mantle lithosphere that is  $\sim 1.5\%$  enriched in magnesium relative to the Mesoproterozoic Mazatzal block (Figure 8b). Following equation (5), this  $20 \text{ kg/m}^3$  compositional difference supports more than 500 meters of topography in the Superior province, a similar (if not more modest) magnitude to that proposed for the Archean Wyoming craton [Hasterok and Chapman, 2007; Levandowski et al., 2014]. A broader study of this kind that includes regions of much younger tectonic age could potentially establish a more robust baseline for inferring variations in mantle depletion.

The interpretation that the density of the mantle beneath the MCR is unrelated to rifting accords with geochemical evidence that high-temperature melting of the mantle lithosphere by an impinging mantle plume was not the primary magma source. Nevertheless, the  $\sim 6$  Myr hiatus in volcanism is challenging to explain with far-field stress alone.

Based on the temporal progression in the magma source depth and composition we propose that phase changes within the primitive mantle material created a positive feedback between lithospheric extension and mantle upwelling. Early-phase magmas tapped near-primitive ( $\epsilon_{\text{Nd}} \sim 0$ ) garnet pyroxenite and garnet peridotite at 100–200 km depth, near the base of the lithosphere; 6 Myr later, however, spinel peridotite was the main magma source, with melting depths of 40–70 km [Nicholson et al., 1997].

The fact that early and main-stage volcanism did not sample the mantle lithosphere and was not contaminated by crustal material suggests that efficient conduits (such as in a lithospheric-scale fracture zone that

was accommodating extension in response to far-field stress) passed decompression-melts of primitive mantle material to the surface. Such extension would also accommodate the upwelling of the underlying primitive material.

As the lithosphere continued to thin, however, the rising material would have crossed the garnet-spinel phase transition at ~100 km, with two effects. First, the loss of garnet would reduce the density of the upwelling material, providing additional buoyancy force. Since we envision that the extension of the lithosphere availed the primitive material accommodation space, this increased buoyancy would be uniquely focused beneath the rift. The increased elevation and thus gravitational potential energy of the rift would further encourage and further focus extension. Second, the phase transition from garnet to spinel increases the peridotite solidus temperature at a given pressure [Green and Ringwood, 1967b], or conversely lowers solidus pressure at a given temperature. Therefore, the primitive material would cease to melt even though it continued to rise. Melting did not resume until the lithosphere had thinned sufficiently due to the combination of far-field stress and gravitational collapse to allow the primitive material to reach the 40–70 km source depth of the main phase volcanics [Nicholson et al., 1997].

#### 8.4. Lithostatic Pressure Gradients Encouraged Postriifting Contraction

While the existing faults and the warm crust and upper mantle beneath the rift would have been less resistant to horizontal shortening, it is also likely that gravitational body forces—those due to lateral lithostatic pressure disequilibria—further nucleated contraction in the MCR itself. In essence, the lithostatic pressure(s) adjacent to a point can be viewed as confining stress. If the pressures are equal, that point is duly confined, but adjacent pressure-deficits result in a horizontal tensile stress, and pressure-excesses compression. The deviatoric stress due to body forces is normal to the pressure contrast and has an average magnitude from the surface and depth  $z_{bottom}$  equal to the depth-averaged lithostatic pressure contrast [Tappognier and Molnar, 1976]:

$$\sigma_{body} = \frac{1}{z_{bottom}} \int_{surface}^{z_{bottom}} \Delta P(z) dz = \int_{surface}^{z_{bottom}} \left( \int_{surface}^z \Delta \rho g z' dz' \right) dz \quad (10)$$

Low pressure (i.e., low density or elevation) regions are less resistant to contraction than regions of high pressure, in which extension is favored.

The MCR was a local basin throughout the period of extension [Cannon, 1994]. Even if the basin had been filled entirely by the end of rifting, and therefore there was no topographic contribution to lithostatic pressure gradient across the MCR, the lateral density contrast between ~2300 kg/m<sup>3</sup> sediment and ~2700 kg/m<sup>3</sup> continental upper crust would generate a pressure difference of 20 MPa by 5 km depth. If this material were underlain by 2900 kg/m<sup>3</sup> intrusions beneath the rift and 2800 kg/m<sup>3</sup> crystalline rock outside of the rift, the pressure would equalize by 25 km depth. These densities and thicknesses are simply crude approximations based on the model of Cannon [1994], but note that the topography supported by both of these theoretical columns is equal (equation (4)). Nevertheless by equation (10), the average pressure through the upper crust would have been 10 MPa less in the rift than beneath the flanks: Independent of the existence of faults and the increased temperature beneath the MCR, density structure within the MCR at the cessation of rifting would have augmented rift-normal far-field compression by 10 MPa in the upper crust. Again, these values are based on only a crude estimate of the density structure at the end of extension, but it is axiomatic that the average lithostatic pressure in the upper crust is less beneath a sedimentary basin than adjacent crystalline terranes. Consequently, the density structure near the MCR must have encouraged postriifting contractual reactivation of normal faults.

#### 8.5. Implications for Modern Intraplate Seismicity in Ancient Rifts

The MCR was a major continental rift that cut across the existing structural grain and therefore likely did not exploit an antecedent zone of weakness. The inferences that we draw from the density structure in the region surrounding the MCR support the view that the initiation of tectonism in continental interiors is not contingent upon favorable asthenospheric convective regimes or anomalously low viscosity or friction in fault zones. Additionally, subsequent deformation—such as postriifting contraction in warm and extended lithosphere—may not only act upon locally anomalous rheologies but also may be localized by lithostatic pressure gradients.

The implication of this prospect is that loci of modern intraplate strain need not be subjected to anomalous contemporary boundary forces, especially if previous tectonism has created large lateral density contrasts.

In the ancient rifts specifically, there likely remain large pressure contrasts between the rift and its flanks, but the magnitude and polarity of these gradients varies, as does the result of their interaction with far-field stress. For example, while the MCR is now a lithostatic pressure high, the Mississippi Embayment is a topographic low covered by several kilometers of sediment [Frezon *et al.*, 1988]. The NE trend of these and other central-eastern North American rifts is subparallel to the long-wavelength NE-SW maximum horizontal compressive stress [e.g., Zoback and Zoback, 1980; Hurd and Zoback, 2012]. Body-force derived stress sums with this regional stress field and may reorient maximum horizontal compressive stress to be either better (in the case of the Mississippi Embayment [Grana and Richardson, 1996]) or more poorly (MCR) oriented relative to rift-related faults. Therefore, the density structure inherited from previous rifting may either encourage or discourage seismicity on rift-parallel faults.

Indeed, although much of the historical seismicity in central and eastern North America occurs in or near rifted zones (e.g., the Reelfoot rift, Atlantic margin, and St. Lawrence rift), there are zones of previous extensional tectonism—exemplified by the MCR—that are historically seismically quiescent. Considering the end-member examples mentioned above, we submit that in order to understand the spatial distribution of seismicity in continental interiors, it is crucial not simply to document the tectonic history of a region but rather to evaluate the physical interactions among far-field stress and the faults and density structure inherited from prior tectonism.

## 9. Future Applications

The algorithm developed here generates lithospheric density models that are mutually consistent with seismic velocity, gravity, heat flow and topography. Comparison of these density models with seismic velocity has proven useful and effective in exploring variations in mantle lithospheric chemistry and the kinematics of a failed continental rift.

Two specific seismic models will be useful in future work. In the MCR, preliminary tomographic models [Aleqabi *et al.*, 2013; Bollmann *et al.*, 2013] from the SPREE deployment [Stein, 2011] reveal intriguing variations in  $v_p$ ,  $v_s$ , and  $v_p/v_s$ . These quantities provide complementary constraints on interpreting crustal lithologic variations, since compositional differences affect shear and compressional velocities differently and the biases of  $v_p$ -density scaling differ from those of S-velocities [Humphreys and Dueker, 1994; Levandowski *et al.*, 2013].

On a broad scale, uniformly generated seismic velocity and crustal thickness models from the entire Transportable Array footprint [Shen *et al.*, 2013c] could be used to generate continental-scale density models of the continental United States in a uniform way; jointly, these velocity and density models could improve our understanding of tectonic evolution, lithology and the state of stress in this intraplate environment. For example, it has been postulated that mantle flow (i.e., dynamic topography) may modify surface elevation, depressing the Mississippi Embayment [Forte *et al.*, 2007] and/or raising the Appalachians [Gallen *et al.*, 2013; Miller *et al.*, 2013]. Such dynamic topography would manifest in seismically derived density estimates that recover gravity variations but fail to match topography. Second, density models can be used to interrogate the process of continental rifting and the fate of such rifts, not only in the seismically quiet MCR [e.g., Bartz *et al.*, 2014] but also in the seismically active Reelfoot rift and Atlantic passive margin. Such models could explore whether there is a connection between rift-related structures and the pattern of historical seismicity. Third, crustal velocity and density models can highlight variations in crustal lithology, from which differences in rheology can be inferred. Such differences have been invoked as controls on intraplate strain localization [Liu and Zoback, 1997; Pollitz *et al.*, 2001; Pollitz and Mooney, 2013]. Lastly, a comprehensive map of the stress due to lithostatic pressure variations, coupled with derived lithologic and rheologic information, may provide insight into the cause of intraplate seismicity and inform seismic hazard assessment in the central and eastern United States.

## 10. Conclusion

A new technique has been developed to use seismic velocity models and the differing sensitivities of gravity and flexural topography to estimate crustal and upper mantle density. The resultant density model provides information on crustal and mantle lithology not revealed by uniform seismic velocity-to-density scaling relations.

Density models of the western arm of the Midcontinent Rift are more consistent with a passive rift generated by far-field tension than a thermal-plume driven active rift. Specifically, mantle density variations that are inferred to arise from composition record pre rift depletion and thus limited lithospheric melting during synrift magmatism. Following extension, inversion of normal faults thickened the crust in and near the rift. This reactivation exploited existing weakness in warm, recently faulted lithosphere but was also facilitated by a gravitational potential energy low in the extended zone. While this crustal thickening increased the buoyancy of the rift's flanks, high-density lowermost crust now beneath the rift suggests that the lower part of the suite of intrusive mafic rocks was advected downward to eclogite facies.

With this new, efficient algorithm to extract 3-D density models from geophysical data, uniformly processed seismic models covering large regions will allow critical comparisons between seismic velocity and density, lending new insights into important tectonic and geodynamic questions at local, regional, and continental scales.

#### Acknowledgments

The U.S. Geological Survey Mendenhall Postdoctoral Program funded WBL's contribution to this work as part of the Central and Eastern US seismic hazard program. Weisen Shen shared the seismic velocity models. Fred Pollitz, Suzanne Nicholson, and Morgan Moschetti conducted presubmission reviews. Associate Editor Cin-Ty Lee provided additional comments. C. Shepherd is thanked for an informative tour of MCR geology. The full posterior distributions of density models, as well as the mean model, are available as supporting information. The full set of MATLAB scripts used to build the starting model and the simulated annealing algorithm are also included therein. Any use of trade, product, or firm names is for descriptive purposes only and does not imply endorsement by the U.S. Government.

#### References

- Afonso, J. C., J. Fullea, W. L. Griffin, Y. Yang, A. G. Jones, J. A. D Connolly, and S. Y. O'Reilly (2013), 3-D multiobservable probabilistic inversion for the compositional and thermal structure of the lithosphere and upper mantle. I: a prioripetrological information and geophysical observables, *J. Geophys. Res. Solid Earth*, 118(5), 2586–2617, doi:10.1002/jgrb.50124.
- Afonso, J. C., G. Ranalli, and M. Fernández (2005), Thermal expansivity and elastic properties of the lithospheric mantle: Results from mineral physics of composites, *Phys. Earth Planet. Inter.*, 149(3-4), 279–306, doi:10.1016/j.pepi.2004.10.003.
- Aleqabi, G. I., D. A. Wiens, and M. E. Wyssession (2013), The structure of the mid-continent rift of North America from combined surface wave and ambient noise tomography, Abstract T21B-2547 presented at 2013 Fall Meeting, AGU, San Francisco, Calif.
- Bartz, D., et al. (2014), Assessing microseismicity of the northern mid-continent rift zone and surrounding regions, Abstract T13B-4638 presented at 2014 Fall Meeting, AGU, San Francisco, Calif.
- Behn, M. D., and P. B. Kelemen (2003), Relationship between seismic P-wave velocity and the composition of anhydrous igneous and meta-igneous rocks, *Geochem. Geophys. Geosyst.*, 4(5), 1041, doi:10.1029/2002GC000393.
- Behrendt, J. C., A. G. Green, W. F. Cannon, D. R. Hutchinson, M. W. Lee, B. Milkereit, W. F. Agena, and C. Spencer (1988), Crustal structure of the Midcontinent rift system: Results from GLIMPCE deep seismic reflection profiles, *Geology*, 16(1), 81–85, doi:10.1130/0091-7613(1988)016<0081:CSOTMR>2.3.CO;2.
- Behrendt, J. C., D. R. Hutchinson, M. Lee, C. R. Thornber, A. Trehu, W. Cannon, and A. Green (1990), GLIMPCE Seismic reflection evidence of deep-crustal and upper-mantle intrusions and magmatic underplating associated with the Midcontinent Rift system of North America, *Tectonophysics*, 173(1-4), 595–615, doi:10.1016/0040-1951(90)90248-7.
- Blakely, R. J. (1996), Potential theory in gravity and magnetic applications, Cambridge University Press.
- Blackwell, D. D., and M. C. Richards (2004), *Geothermal Map of North America*, 1 sheet, scale 1:6,500,000, American Association of Petroleum Geologists (AAPG), Tulsa, Okla.
- Bollmann, T., S. van der Lee, and A. W. Frederiksen (2013), Preliminary results of P&S wave teleseismic tomography of the Superior region, Abstract T23B-2578 presented at 2013 Fall Meeting, AGU, San Francisco, Calif.
- Bornhorst, T. J., J. B. Paces, N. K. Grant, J. D. Obradovich, and N. K. Huber (1988), Age of native copper mineralization, Keweenaw Peninsula, Michigan, *Econ. Geol.*, 83(3), 619–625, doi:10.2113/gsecongeo.83.3.619.
- Bouhifd, M. A., D. Andrault, G. Fiquet, and P. Richet (1996), Thermal expansion of forsterite up to the melting point, *Geophys. Res. Lett.*, 23(10), 1143–1146, doi:10.1029/96GL01118.
- Boyd, F. R. (1989), Compositional distinction between oceanic and cratonic lithosphere, *Earth Planet. Sci. Lett.*, 96(1-2), 15–26, doi:10.1016/0012-821X(89)90120-9.
- Brocher, T. M. (2005), Empirical relations between elastic wavespeeds and density in the earth's crust, *Bull. Seismol. Soc. Am.*, 95(6), 2081–2092, doi:10.1785/0120050077.
- Cannon, W. F. (1994), Closing of the Midcontinent rift-A far-field effect of Grenvillian compression, *Geology*, 22(2), 155–158, doi:10.1130/0091-7613(1994)022<0155:COTMRA>2.3.CO;2.
- Cannon, W. F., and W. J. Hinze (1992), Speculations on the origin of the North American Midcontinent rift, *Tectonophysics*, 213(1-2), 49–55, doi:10.1016/0040-1951(92)90251-Z.
- Christensen, N. I. (1996), Poisson's ratio and crustal seismology, *J. Geophys. Res.*, 101(B2), 3139–3156, doi:10.1029/95JB03446.
- Christensen, N. I., and W. D. Mooney (1995), Seismic velocity structure and composition of the continental crust: A global view, *J. Geophys. Res.*, 100(B6), 9761–9788.
- Dater, D., D. Metzger, and A. Hittelman (1999), *Dater: Land and Marine Gravity* [CD-ROM], Natl. Geophys. Data Cent., Boulder, Colo.
- Davis, D. W., and J. C. Green (1997), Geochronology of the North American Midcontinent rift in western Lake Superior and implications for its geodynamic evolution, *Can. J. Earth Sci.*, 34(4), 476–488, doi:10.1139/e17-039.
- DeNosaquo, K. R., R. B. Smith, and A. R. Lowry (2009), Density and lithospheric strength models of the Yellowstone–Snake River Plain volcanic system from gravity and heat flow data, *J. Volcanol. Geotherm. Res.*, 188(1-3), 108–127, doi:10.1016/j.jvolgeores.2009.08.006.
- Ellam, R. M., R. W. Carlson, and S. B. Shirey (1992), Evidence from Re-Os isotopes for plume–lithosphere mixing in Karoo flood basalt genesis, *Nature*, 359, 718–721, doi:10.1038/359718a0.
- Forte, A. M., J. X. Mitrovica, R. Moucha, N. A. Simmons, and S. P. Grand (2007), Descent of the ancient Farallon slab drives localized mantle flow below the New Madrid seismic zone, *Geophys. Res. Lett.*, 34, L04308, doi:10.1029/2006GL027895.
- Frederiksen, A. W., T. Bollmann, F. Darbyshire, and S. van der Lee (2013), Modification of continental lithosphere by tectonic processes: A tomographic image of central North America, *J. Geophys. Res. Solid Earth*, 118, 1051–1066, doi:10.1002/jgrb.50060.
- Frezon, S. E., T. M. Finn, and K. L. Varnes (1988), *Map of Sedimentary Basins in the Conterminous United States*.
- Gallen, S. F., K. W. Wegmann, and D. R. Bohnenstiehl (2013), Miocene rejuvenation of topographic relief in the southern Appalachians, *GSA Today*, 23(2), 4–10, doi:10.1130/GSATG163A.1.

- Godey, S., F. Deschamps, J. Trampert, and R. Snieder (2004), Thermal and compositional anomalies beneath the North American continent, *J. Geophys. Res.*, 109, B01308, doi:10.1029/2002JB002263.
- Goff, J. A., K. Holliger, and A. Levander (1994), Modal fields: A new method for characterization of random seismic velocity heterogeneity, *Geophys. Res. Lett.*, 21(6), 493–496.
- Gordon, M. B., and M. R. Hempton (1986), Collision-induced rifting: The Grenville Orogeny and the Keweenawan Rift of North America, *Tectonophysics*, 127(1-2), 1–25, doi:10.1016/0040-1951(86)90076-4.
- Grana, J. P., and R. M. Richardson (1996), Tectonic stress within the New Madrid seismic zone, *J. Geophys. Res.*, 101(B3), 5445–5458.
- Green, D. H., and A. E. Ringwood (1967a), An experimental investigation of the gabbro to eclogite transformation and its petrological applications, *Geochim. Cosmochim. Acta*, 31(5), 767–833, doi:10.1016/S0016-7037(67)80031-0.
- Green, D. H., and A. E. Ringwood (1967b), The stability fields of aluminous pyroxene peridotite and garnet peridotite and their relevance in upper mantle structure, *Earth Planet. Sci. Lett.*, 3, 151–160, doi:10.1016/0012-821X(67)90027-1.
- Green, J. C. (1982), Geology of Keweenawan extrusive rocks, in *Geology and Tectonics of the Lake Superior Region*, GSA Mem. 156, 47–56, edited by R. J. Wold and W. J. Hinze, Boulder, Colo.
- Hammond, W. C., and E. D. Humphreys (2000), Upper mantle seismic wave attenuation: Effects of realistic partial melt distribution, *J. Geophys. Res.*, 105(B5), 10,975–10,986.
- Hasterok, D., and D. S. Chapman (2007), Continental thermal isostasy: 2. Application to North America, *J. Geophys. Res.*, 112, B06415, doi:10.1029/2006JB004664.
- Hawkesworth, C. J., K. Gallagher, S. Kelley M. Mantovani, D. W. Peate, M. Regelous, and N. W. Rogers (1992), Paraná magmatism and the opening of the South Atlantic, *Geol. Soc. Spec. Publ.*, 68, 221–240.
- Holliger, K., A. R. Levander, and J. A. Goff (1993), Stochastic modeling of the reflective lower crust: Petrophysical and geological evidence from the Ivera Zone (Northern Italy), *J. Geophys. Res.*, 98(B7), 11,967–11,980.
- Hugh-Jones, D. (1997), Thermal expansion of MgSiO<sub>3</sub> and FeSiO<sub>3</sub> ortho-and clinopyroxenes, *Am. Mineral.*, 82, 689–696.
- Humphreys, E. D., and K. G. Dueker (1994), Physical state of the western U.S. upper mantle, *J. Geophys. Res.*, 99(B5), 9615–9634.
- Hurd, O., and M. D. Zoback (2012), Intraplate earthquakes, regional stress and fault mechanics in the Central and Eastern U.S. and South-eastern Canada, *Tectonophysics*, 581, 182–192, doi:10.1016/j.tecto.2012.04.002.
- Hutchinson, D. R., R. S. White, W. F. Cannon, and K. J. Schulz (1990), Keweenaw hot spot: Geophysical evidence for a 1.1 Ga mantle plume beneath the Midcontinent Rift System, *J. Geophys. Res.*, 95(B7), 10,869–10,884.
- Jackson, I., and U. H. Faul (2010), Grainsize-sensitive viscoelastic relaxation in olivine: Towards a robust laboratory-based model for seismological application, *Phys. Earth Planet. Inter.*, 183(1-2), 151–163, doi:10.1016/j.pepi.2010.09.005.
- Jackson, J. M., J. W. Palko, D. Andrault, S. V. Sinogeikin, D. L. Lakshtanov, J. Wang, J. D. Bass, and C.-S. Zha (2003), Thermal expansion of natural orthoenstatite to 1473 K, *Eur. J. Mineral.*, 15(3), 469–473, doi:10.1127/0935-1221/2003/0015-0469.
- Jones, C. H., J. R. Unruh, and L. J. Sonder (1996), The role of gravitational potential energy in active deformation in the southwestern United States, *Nature*, 381, 1–5.
- Jordan, T. H. (1975), The continental tectosphere, *Rev. Geophys.*, 13(3), 1–12, doi:10.1029/RG013i003p00001.
- Jordan, T. H. (1978), Composition and development of the continental tectosphere, *Nature*, 10, 554–548.
- Jordan, T. H. (1979), Mineralogies, densities and seismic velocities of garnet lherzolites and their geophysical implications, in *The Mantle Sample: Inclusion in Kimberlites and Other Volcanics*, edited by F.R. Boyd and H. O.A. Meyer, AGU, Washington, D. C.
- Kaban, M. K., P. Schwintzer, I. M. Artemieva, and W. D. Mooney (2003), Density of the continental roots: compositional and thermal contributions, *EPSL*, 209(1-2), 53–69, doi:10.1016/S0012-821X(03)00072-4.
- Kaban, M. K., M. Tesauro, W. D. Mooney, and S. A. P. L. Cloetingh (2014), Density, temperature, and composition of the North American lithosphere—New insights from a joint analysis of seismic, gravity, and mineral physics data: 1. Density structure of the crust and upper mantle, *Geochem. Geophys. Geosyst.*, 15, 4781–4807, doi:10.1002/2014GC005483.
- Kent, R. W., M. Storey, and A. D. Saunders (1992), Large igneous provinces: Sites of plume impact or plume incubation?, *Geology*, 20(10), 891–894, doi:10.1130/0091-7613(1992)020<0891:LIPSOP>2.3.CO;2.
- Kirby, J. F., and C. J. Swain (2009), A reassessment of spectral Te estimation in continental interiors: The case of North America, *J. Geophys. Res.*, 114, B08401, 39–62, doi:10.1029/2009JB006356.
- Lachenbruch, A. H., and P. Morgan (1990), Continental extension, magmatism and elevation: formal relations and rules of thumb, *Tectonophysics*, 174(1-2), doi:10.1016/0040-1951(90)90383-J.
- Lee, C.-T. A. (2003), Compositional variation of density and seismic velocities in natural peridotites at STP conditions: Implications for seismic imaging of compositional heterogeneities in the upper mantle, *J. Geophys. Res.*, 108(B9), 2441, doi:10.1029/2003JB002413.
- Levandowski, W., C. H. Jones, H. Reeg, A. Frassetto, H. Gilbert, G. Zandt, and T. J. Owens (2013), Seismological estimates of means of isostatic support of the Sierra Nevada, *Geosphere*, 9(6), 1552–1561, doi:10.1130/GES00905.1.
- Levandowski, W., C. H. Jones, W. Shen, M. H. Ritzwoller, and V. Schulte-Pelkum (2014), Origins of topography in the western U.S.: Mapping crustal and upper mantle density variations using a uniform seismic velocity model, *J. Geophys. Res. Solid Earth*, 119, 2375–2396, doi:10.1002/2013JB010607.
- Liu, L., and M. D. Zoback (1997), Lithospheric strength and intraplate seismicity in the New Madrid seismic zone, *Tectonics*, 16(4), 585–595, doi:10.1029/97TC01467.
- Matsukage, K. N., Y. Nishihara, and S.-I. Karato (2005), Seismological signature of chemical differentiation of Earth's upper mantle, *J. Geophys. Res.*, 110, B12305, doi:10.1029/2004JB003504.
- McWilliams, M. O., and D. J. Dunlop (1978), Grenville paleomagnetism and tectonics, *Can. J. Earth Sci.*, 15(5), 687–695, doi:10.1139/e78-076.
- Merino, M., G. R. Keller, S. Stein, and C. Stein (2013), Variations in Mid-Continent Rift magma volumes consistent with microplate evolution, *Geophys. Res. Lett.*, 40, 1513–1516, doi:10.1002/grl.50295.
- Miller, J. D., J. C. Green, M. J. Severson, V. W. Chandler, S. A. Hauck, D. M. Peterson, and T. E. Wahl (2002), *Geology and Mineral Potential of the Duluth Complex and Related Rocks of Northeastern Minnesota*, Minn. Geol. Surv., St. Paul, Minn.
- Miller, S. R., P. B. Sak, E. Kirby, and P. R. Bierman (2013), Neogene rejuvenation of central Appalachian topography: Evidence for differential rock uplift from stream profiles and erosion rates, *Earth Planet. Sci. Lett.*, 369–370, 1–12, doi:10.1016/j.epsl.2013.04.007.
- Mooney, W. D., and M. K. Kaban (2010), The North American upper mantle: Density, composition, and evolution, *J. Geophys. Res.*, 115, B12424, doi:10.1029/2010JB000866.
- Nicholson, S. W., and S. B. Shirey (1990), Midcontinent rift volcanism in the Lake Superior Region: Sr, Nd, and Pb isotopic evidence for a mantle plume origin, *J. Geophys. Res.*, 95(B7), 10,851–10,868, doi:10.1029/JB095iB07p10851.
- Nicholson, S. W., K. J. Schulz, S. B. Shirey, and J. C. Green (1997), Rift-wide correlation of 1.1 Ga Midcontinent rift system basalts: Implications for multiple mantle sources during rift development, *Can. J. Earth Sci.*, 34(4), 504–520, doi:10.1139/e17-041.

- Paces, J. B. (1988), Magmatic processes, evolution, and mantle sources contributing to the petrogenesis of Midcontinent Rift basalts: Portage Lake Volcanics, Keweenaw Peninsula, Michigan, PhD dissertation. Mich. Technol. Univ., Houghton.
- Paces, J. B., and J. D. Miller (1993), Precise U-Pb ages of Duluth Complex and related mafic intrusions, northeastern Minnesota: Geochronological insights to physical, petrogenetic, paleomagnetic, and tectonomagmatic processes associated with the 1.1 Ga Midcontinent Rift System, *J. Geophys. Res.*, 98(B8), 13,997–14,013, doi:10.1029/93JB01159.
- Pedersen, T., and H. E. Ro (1992), Finite duration extension and decompression melting, *Earth Planet. Sci. Lett.*, 113(1-2), 15–22, doi:10.1016/0012-821X(92)90208-D.
- Pollitz, F. F., and W. D. Mooney (2013), Seismic structure of the Central US crust and shallow upper mantle: Uniqueness of the Reelfoot Rift, *Earth Planet. Sci. Lett.*, 402, 157–166, doi:10.1016/j.epsl.2013.05.042.
- Pollitz, F. F., L. Kellogg, and R. Burgmann (2001), Sinking mafic body in a reactivated lower crust: A mechanism for stress concentration at the New Madrid seismic zone, *Bull. Seismol. Soc. Am.*, 91, 1–37.
- Roca, E. (2001), The Northwest Mediterranean basin (Valencia Trough, Gulf of Lions and Liguro-Provençal basins): Structure and geodynamic evolution, in *Peritheyan Rift/Wrench Basins and Passive Margins*, vol. 186, edited by P. A. Ziegler et al., pp. 671–706, Mém. Mus. Natl. Histoire Nat., Paris.
- Rudnick, R. L., and D. M. Fountain (1995), Nature and composition of the continental crust: A lower crustal perspective, *Rev. Geophys.*, 33(3), 267–309.
- Saunders, A. D., M. Storey, and R. W. Kent (1992), Consequences of plume-lithosphere interactions, *Geol. Soc. Spec. Publ.*, 68, 41–60.
- Schutt, D. L., and C. E. Lesser (2010), Compositional trends among Kaapvaal Craton garnet peridotite xenoliths and their effects on seismic velocity and density, *Earth Planet. Sci. Lett.*, 300(3-4), 367–373, doi:10.1016/j.epsl.2010.10.018.
- Serpa, L., T. Setzer, H. Farmer, L. Brown, J. Oliver, S. Kaufman, J. Sharp, and D. W. Steeles (1984), Structure of the Southern Keweenawan Rift from COCORP Surveys across the midcontinent geophysical anomaly in northeastern, Kansas, *Tectonics* v., 3, 367–384.
- Shen, W., M. H. Ritzwoller, and V. Schulte-Pelkum (2013a), A 3-D model of the crust and uppermost mantle beneath the Central and Western US by joint inversion of receiver functions and surface wave dispersion, *J. Geophys. Res. Solid Earth*, 118, 262–276, doi:10.1029/2012JB009602.
- Shen, W., M. H. Ritzwoller, and V. Schulte-Pelkum (2013b), Crustal and uppermost mantle structure in the central U.S. encompassing the Midcontinent Rift, *J. Geophys. Res. Solid Earth*, 118, 4325–4344, doi:10.1002/jgrb.50321.
- Shen, W., M. H. Ritzwoller, J. Xie, Y. Zheng, Z. Xu, and L. Zhou (2013c), Aspects of surface wave tomography across CEArray and USArray, Abstract S53A-2397 presented at 2013 Fall Meeting, AGU, San Francisco, Calif.
- Sheehan, A. F., and S. C. Solomon. (1991), Joint inversion of shear wave travel time residuals and geoid and depth anomalies for long-wavelength variations in upper mantle temperature and composition along the Mid-Atlantic Ridge *JGR*, 96(B12), 19981–20009, doi:10.1029/91JB01988.
- Shirey, S. B., K. W. Klewin, J. H. Berg, and R. W. Carlson (1994), Temporal changes in the sources of flood basalts: Isotopic and trace element evidence from the 1100 Ma old Keweenawan Mamainse Point Formation, Ontario, Canada, *Geochim. Cosmochim. Acta*, 58(20), 4475–4490, doi:10.1016/0016-7037(94)90349-2.
- Stein, C. A., S. Stein, M. Merino, G. Randy Keller, L. M. Flesch, and D. M. Jurdy (2014), Was the Midcontinent Rift part of a successful seafloor-spreading episode?, *Geophys. Res. Lett.*, 41, 1465–1470, doi:10.1002/2013GL059176.
- Stein, S. (2011), Learning from failure: The SPREE Mid-Continent Rift Experiment, *GSA Today*, 21(9), 5–7, doi:10.1130/G120A.1.
- Tapponnier, P., and P. Molnar (1976), Slip-line field theory and large-scale continental tectonics, *Nature*, 264(5584), 319–324, doi:10.1038/264319a0.
- van der Lee, S., and G. Nolet (1997), Upper mantle S velocity structure of North America, *J. Geophys. Res.*, 102(B10), 22,815–22,838.
- Vervoort, J. D., K. Wirth, B. Kennedy, T. Sandland, and K. S. Harpp (2007), The magmatic evolution of the Midcontinent rift: New geochronologic and geochemical evidence from felsic magmatism, *Precambrian Res.*, 157(1-4), 235–268, doi:10.1016/j.precamres.2007.02.019.
- Watts, A. B. (2001), *Watts: Isostasy and Flexure of the Lithosphere*, Cambridge University Press, Cambridge, U. K.
- Watts, A. B. (2012), Global elastic thickness point data and grid. [Available at earth.ox.ac.uk/tony/watts/downloads.htm, last accessed 6/1/2012.]
- Weiblen, P. W., and G. B. Morey (1980), A summary of the stratigraphy, petrology, and structure of the Duluth Complex, *Am. J. Sci.*, 280(A), 88–133.
- Weiss, T., S. Siegesmund, W. Rabbel, T. Bohlen, and M. Pohl (1999), Seismic velocities and anisotropy of the lower continental crust: A review, *Pure Appl. Geophys.*, 156, 97–122.
- White, R., and D. McKenzie (1989), Magmatism at rift zones: The generation of volcanic continental margins and flood basalts, *J. Geophys. Res.*, 94(B6), 7685–7729.
- Wirth, K. R., Z. J. Naiman, and J. D. Vervoort (1997), The Chengwatana Volcanics, Wisconsin and Minnesota: Petrogenesis of the southernmost volcanic rocks exposed in the Midcontinent rift, *Can. J. Earth Sci.*, 34(4), 536–548, doi:10.1139/e97-043.
- Woelk, T. S., and W. J. Hinze (1991), Model of the midcontinent rift system in northeastern Kansas, *Geology*, 19(3), 277–280.
- Ziegler, P. A. (1988), Evolution of the Arctic-North Atlantic and the western Tethys—A visual presentation of a series of paleogeographic paleotectonic maps\*, *Mem Am. Assoc. Pet. Geol.*, 43, 164–196.
- Ziegler, P. A., and S. Cloetingh (2004), Dynamic processes controlling evolution of rifted basins, *Earth Sci. Rev.*, 64(1-2), 1–50, doi:10.1016/S0012-8252(03)00041-2.
- Zoback, M. L., and M. D. Zoback (1980), State of stress in the conterminous United States, *J. Geophys. Res.*, 85(11), 6113–6156.